GEORG-AUGUST-UNIVERSITÄT GÖTTINGEN

Uploaddatum: 11.07.2026
Uploadzeit: 11:36

Dies ist ein von FlexNow automatisch beim Upload generiertes Deckblatt. Es dient dazu, die Arbeit automatisiert der Prüfungsakte zuordnen zu können.

**This is a machine generated frontpage added by FlexNow.
Its purpose is to link your upload to your examination file.**

Matrikelnummer: 26242241



GEORG-AUGUST-UNIVERSITÄT GÖTTINGEN IN PUBLICA COMMODA SEIT 1737

Fakultät für Physik [q,p]=iℏ

Bachelor's Thesis

Untersuchung eines grundlegenden Modells für generische $t\bar{t} + X$ Ereignis Rekonstruktion im ATLAS Experiment

Studies of a Foundational Model for Generic $t\bar{t} + X$ Event Reconstruction in ATLAS

prepared by

Mark Brandau

from Kassel

at the II. Physikalischen Institut

Thesis number:	II.Physik-UniGö-BSc-2026/07
Thesis period:	6th April 2014 until 10th July 2026
First referee:	Prof. Dr. Quadt
Second referee:	Prof. Dr. Frey

Zusammenfassung

Das Top-Quark ist das Elementarteilchen mit der größten Masse im Standardmodell. Da die mittlere Lebensdauer des Top-Quarks kürzer als die Zeitspanne auf der Hadronisierung stattfindet ist, ist das Top-Quark besonders interessant für physikalische Untersuchungen. In $t\bar{t}$ Paarproduktion durch Gluon-Gluon Fusion können zusätzliche Bosonen wie W, γ, Z, H erzeugt werden. Solche Prozesse werden als $t\bar{t} + X$ Prozesse bezeichnet. Für die Klassifizierung solcher Prozesse sind Graph Neural Networks besonders geeignet, da sich die Struktur von den Events im Detektor gut als Graph darstellen lässt. Mit einer Monte-Carlo-Simulation werden die Datensätze für das Training bereitgestellt. Das Netz rekonstruiert die Flavour der erzeugten Partonen des Prozesses und ob die Partonen vom selben Mutterteilchen stammen. Wenn die Partonen aus dem selben Mutterteilchen zerfallen sind, sagt das Netz auch welches Mutterteilchen es war.

Stichwörter: $t\bar{t} + X$ Prozess, ATLAS, Top Quark, Graph Neural Network

Abstract

The top quark is the elementary particle with the largest mass in the Standard Model. Being shorter than the hadronisation time, the mean lifetime of the top quark makes it particularly interesting for a physical analysis because this enables the measurement of bare quarks. In $t\bar{t}$ pair production, additional bosons such as W, Z, γ, H can be produced. These kinds of processes are so-called $t\bar{t} + X$ processes. For the classification of such processes, Graph-Neural-Networks are especially suitable because the structure of events in the detector can be naturally embedded in a graph. The data used for training the network is provided by a Monte-Carlo simulation. The model predicts the flavour of the different partons and whether they originated from the same mother particle. If they are connected in this manner, the model also predicts the flavour of the mother particle.

Keywords: $t\bar{t} + X$ process, ATLAS, Top quark, Graph-Neural-Network

Contents

1. Introduction **1**

2. The Standard Model of Particle Physics **3**
2.1. Foundations of the Standard Model 3
2.2. Top-Antitop Production in Association with Bosons 5

3. Experimental Setup **7**
3.1. The Large Hadron Collider 7
3.2. The ATLAS Experiment 7

4. The Top Quark and how to Reconstruct it **9**
4.1. Top Quark Physics 9
4.2. Graph Neural Networks 9
4.3. State of $t\bar{t} + X$ Measurements in ATLAS 10
4.4. Current State in Top Quark Event Reconstruction 11

5. Machine Learning Methodology **13**
5.1. Preprocessing 13
5.2. Training the Network 15
5.3. Loss Curve 16

6. Results **17**
6.1. Studies of the Output Scores 18
6.2. Confusion Matrices 19
6.3. Comparison to Other Algorithms 22

7. Summary and Outlook **27**

A. Branches Preprocessing **33**

B. Edge Output Scores **35**

C. Confusion Matrices **39**

D. Event Depictions **47**

E. ΔR and m_{inv} Distributions **49**

1. Introduction

Particle physics aims to describe the interactions of the elementary components in our universe. The most profound theory today is the Standard Model of particle physics (SM). Worldwide experiments are conducted to probe the parameters of the SM and search for new phenomena beyond it. One of these experimental facilities is CERN, where an incredible number of protons are brought to collision inside four experiments by the Large Hadron Collider (LHC). It is the largest and most energetic particle accelerator ever built, providing a centre-of-mass energy of up to $\sqrt{s} = 13.6\,\text{TeV}$.
Multipurpose detectors like ATLAS are built to detect particles created by these collisions. In 1995, the DØ and CDF detectors at FERMILAB discovered the top quark via $p\bar{p}$ collisions with $\sqrt{s} = 1.8\,\text{TeV}$. The top quark is the most massive elementary particle known today [1] and is therefore of special research interest. The top quark is either produced in single top events or via $t\bar{t}$ pair production.
In addition to the $t\bar{t}$ pair, bosons can be produced. This thesis is concerned with these so-called $t\bar{t}+X$ events, they are used to study the coupling strength of the top to bosons. The different $t\bar{t}+X$ events are $t\bar{t}+H$, $t\bar{t}+\gamma$, $t\bar{t}+W$, and $t\bar{t}+Z$. To classify the different events with higher efficiency, graph-based neural networks (GNNs) are developed. With the approach of supervised machine learning, a GNN is trained to identify flavours and relations of objects in $t\bar{t}+X$ events and classify them into different categories. The node categories are the flavours of the particles and the edge categories are the flavours of the mother particles.
After introducing the SM in Chapter 2 and briefly discussing the LHC and the ATLAS detector in Chapter 3, the topic of my thesis will be elucidated further in Chapter 4. In Chapter 5, the underlying algorithm of the analysis will be illustrated. In Chapter 6 the results of the analysis will be presented and interpreted. In Chapter 7 the work will be summarised, and an outlook for possible improvements will be presented.

2. The Standard Model of Particle Physics

The four known fundamental interactions in our universe are the electromagnetic interaction, the weak interaction, the strong interaction, and the gravitational interaction. The SM incorporates three of the four fundamental interactions but it can not explain gravity on an elementary level. Agreeing with large amounts of data gathered at experiments, the SM is regarded as the state of the art description of fundamental physics. It contains 17 elementary particles, which can be generally divided into fermions and bosons. While fermions are particles with half- integer spin, bosons are particles with integer spin. These particles arise as the excitations of the quantum fields described by the SM. The interactions are described by a Lagrange density [3–13].

2.1. Foundations of the Standard Model

As displayed in Figure 2.1, there are twelve fermions in total and five bosons. Every fermion has an antiparticle which has the same mass as the corresponding particle but discrete quantum numbers of the opposite sign. The fermions also come in three generations and the mass of them increases with higher generations. For every generation there exist two quarks and two leptons each. The fermions can be further divided into quarks and leptons. Quarks carry colour charge and therefore take part in the strong interaction. Every generation has an up-type quark carrying an electric charge of $+\frac{2}{3}$e and a down-type quark with charge $-\frac{1}{3}$e [2]. Because of colour confinement, quarks must form colour neutral bound states with other quarks. These so called hadrons either consist of a quark- antiquark pair (mesons) or baryons with three valence quarks, each having a different colour. In the same way, three antiquarks can form an antibaryon.
Leptons do not carry colour charge and therefore do not interact strongly. They are divided into three electrically neutral neutrinos and three charged leptons, one of them for each generation.

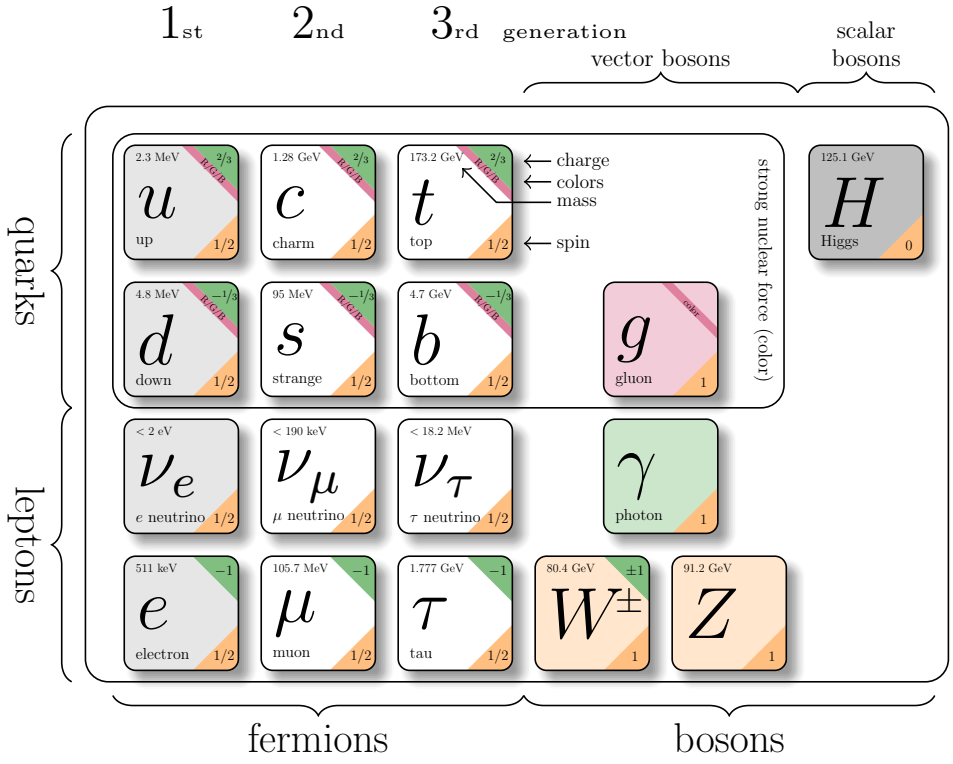


Figure 2.1.: The particle content of the SM. Each particle is labelled via its mass, spin, and if nonzero the corresponding colour charge and electrical charge. Masses and quantum numbers are taken from the PDG [2].

The SM is described by a $\mathrm{SU}(3)_C \times \mathrm{SU}(2)_L \times \mathrm{U}(1)_Y$ symmetry group, where QCD belongs to $\mathrm{SU}(3)_C$ and the electroweak interaction is described by $\mathrm{SU}(2)_L \times \mathrm{U}(1)_Y$ [3–13]. These interactions are mediated by the bosons. They can be subdivided into five vector bosons with spin 1 and one scalar boson with spin 0. The photon, γ, is the massless vector boson of the electromagnetic interaction. It only couples to electrically charged particles. This includes every quark, the charged leptons, and the $W^{\pm}$ bosons of the weak interaction [3–13]. The γ is electrically neutral, hence there is no photon self-coupling. The corresponding quantum field theory for the electromagnetic interaction is quantum electrodynamics (QED), it has a $\mathrm{U}(1)_{\mathrm{EM}}$ gauge symmetry with the weak hypercharge $Y = 2(Q - I_3)$ [3]. In the latter equation, Q is the electrical charge in units of elementary charge and I_3 is the weak isospin.

The gluon, g, is the vector boson of the strong force. It carries both a colour charge and an anticolour charge. The gluon only interacts with colour-charged particles, hence it interacts with quarks and with itself. The latter interaction is of particular interest for

the $t\bar{t}$ production in the LHC because gluon-gluon-fusion is the dominant process for it [14].
The weak interaction is described by quantum flavour dynamics (QFD). It has an $SU(2)_L$ gauge symmetry and is mediated by three vector bosons. Two of them are the charged W^+ and W^- bosons. They have an electrical charge of ± 1 and weak isospin $I_3 = \pm 1$, respectively. They are the force carriers of charged currents and couple to left-handed particles and right-handed antiparticles. The $W^\pm$ can decay into a generation pair of a charged lepton and its corresponding neutrino or into an up- type and down-type quark. In contrast to the leptonic decay, the hadronic decay is able to couple fermions from different generations. The branching ratios of the hadronic decays are described by the Cabibbo-Kobayashi-Maskawa (CKM) Matrix [15, 16]. However, the decays mixing the generations are suppressed. The other mediator of the weak interaction is the electrically neutral Z boson; it is the mediator of neutral currents and has a weak isospin of $I_3 = 0$ [2]. The Z boson does not change flavour and couples to every fermion. Being massive particles, the W and Z bosons both violate the gauge invariance of the SM. The weak bosons also interact with each other, for example via a W^-W^+Z vertex.
The Higgs boson solves the problem of the W and Z masses through the Higgs mechanism and electroweak symmetry breaking [17–19]. H is the only scalar boson in the SM. It carries no electrical charge nor colour charge. It has a mass of $m_H = (125.13 \pm 0.11)\,\text{GeV}$ [2] and has a weak isospin of $I_3 = -\frac{1}{2}$ [2]. Its coupling strength is proportional to the mass of the elementary particle. Therefore it does not couple to the neutrinos [17–19]. Being the most massive particles in the SM, the coupling of a top quark and a Higgs boson is of particular research interest.

2.2. Top-Antitop Production in Association with Bosons

The most common process to yield a $t\bar{t}$ pair in the LHC is the gluon-gluon-fusion (ggf). With a branching ratio of BR(ggf) $\approx 90\%$, it dominates the quark-antiquark annihilation. Alongside this process, additional bosons can be produced. These processes are called $t\bar{t}+X$ events, example leading-order Feynman diagrams are shown in Figure 2.2. Alongside $t\bar{t}$ events with no additional boson, this thesis examines $t\bar{t}Z$ and $t\bar{t}H$ events. The production of a Z boson enables a direct test of neutral-current interactions of the top quark. The decay mode of the Z boson determines the topology of the final state. It can decay into a pair of quarks or leptons. Therefore, the detected objects may include additional jets, isolated leptons, or a significant missing transverse Energy (MET). MET results from

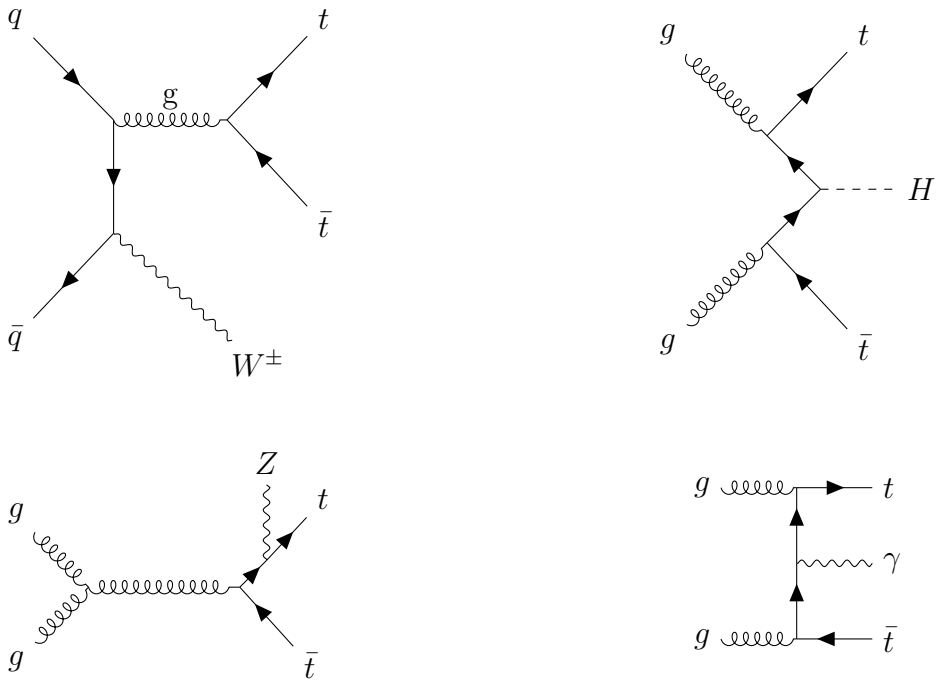


Figure 2.2.: Leading-order example Feynman diagrams for the production modes of $t\bar{t} + X$ events. On the top left an additional $W^{\pm}$ boson is produced, on the top right a H boson, on the bottom left a Z boson and on the bottom right a γ.

particles not detected by the detector. The negative of the measured total transverse momentum is called the missing transverse momentum, in the high-energy limit it is called the missing transverse energy. The Higgs boson in a $t\bar{t}H$ topology provides a direct measurement of the top-Higgs Yukawa coupling, which is the strongest of all fermions because the top quark is the heaviest elementary particle in the SM [1]. This coupling is of great importance for understanding electroweak symmetry breaking and vacuum stability. In this process, the decay of the H defines the topology of the final state. Although it has the largest branching ratio, the mode $H \to b\bar{b}$ has the largest background because of the QCD background. In this decay mode, multiple b jets are to be found in the final state. Another decay mode of importance for this thesis is $H \to WW^*$, this final state is governed by the decay products of the W bosons. Just like the two W bosons from the $t\bar{t}$ decay, they can decay fully hadronic, semileptonic, or dileptonic. Other decay modes of the Higgs include $ZZ^*, \gamma\gamma$, or $\tau\tau$ but are negligible compared to the previously mentioned channels and are therefore not included in this analysis.

3. Experimental Setup

3.1. The Large Hadron Collider

The LHC is the largest synchrotron ever built and provides the highest centre-of-mass energy any accelerator ever achieved. It collides protons and heavy ions at four dedicated collision points. Each of these points hosts an experiment, with ATLAS [20] and CMS [21] being multi-purpose detectors. The other experiments are LHCb, specialised in flavour physics and the ALICE detector, focused on heavy ion collisions.

3.2. The ATLAS Experiment

Coordinate system The coordinate system describing events in the ATLAS experiment has its origin at the interaction point. Tangential to the beam pipe lies the z-axis, while the x-y-plane is perpendicular to the beam pipe with the x-axis pointing to the centre of the LHC. Using cylindrical coordinates, the azimuthal angle, θ, lies between the z-axis and the track of a particle. The polar angle ϕ lies in the x-y-plane and $\phi = 0$ points inwards to the LHC. The pseudorapidity η is defined as:

$$\eta = -\ln\tan\frac{\theta}{2} = \frac{1}{2}\ln\left(\frac{||\vec{p}|| + p_z}{||\vec{p}|| - p_z}\right) \tag{3.1}$$

In high energy physics the relativistic limit of η yields the rapidity

$$y = \frac{1}{2}\ln\left(\frac{E + p_z}{E - p_z}\right). \tag{3.2}$$

This quantity has the advantage of having a Lorentz invariant difference, Δy, for boosts along the beam direction z. Using η and the polar angle ϕ one can compute the angular separation of two particles which is the distance in the pseudorapidity-polar-angle space

$$\Delta R = \sqrt{(\Delta\phi)^2 + (\Delta\eta)^2}. \tag{3.3}$$

Trigger To manage the vast amount of data the 40 MHz collisions produce inside the detector, a trigger system is implemented [20]. This system discards less relevant processes from the ones of interest. It consists of a hardware trigger, the "Level 1 Trigger" and a software trigger, the "High level Trigger". The Level-1 Trigger performs an initial selection by checking whether quantities such as energy, momentum, or missing transverse energy exceed predefined thresholds. Events that pass this stage are then analysed by the High-Level Trigger, which uses more detailed information such as tracking data from the Inner Detector and energy deposits in the calorimeters to make a more refined decision. Events accepted at this stage are ultimately recorded and sent to external storage.

Detector Layers ATLAS is the largest detector at CERN by volume and constructed in concentric layers featuring different detector types. Neighbouring the beam-pipe the Inner Detector (ID) consists of three layers. Due to the high collision rate and limited solid angle, it is finely segmented to handle dense particle activity. High spatial resolution is essential for precise measurement of vertices and interaction points, which is crucial for particle identification and reconstruction. The ID achieves this through a combination of specialised tracking technologies.
The Pixel Detector, located closest to the beam pipe at a radius of about 3 cm, provides highly precise measurements of particle vertex and momentum using roughly 100 million Silicon pixels with a resolution of about 10 μm.
The Semiconductor Tracker (SCT), surrounding the Pixel Detector, reconstructs charged particle tracks with high precision (up to 25 μm) using millions of Silicon detectors arranged in over 4,000 modules.
The Transition Radiation Tracker (TRT), forming the outermost layer, uses around 300,000 gas-filled drift tubes to reconstruct particle tracks and identify particle types using transition radiation.
The Inner Detector is placed inside a superconducting solenoid generating a magnetic field with a strength of 2 T. In the next layer a massive toroidal magnet system is incorporated in the structure, giving ATLAS its name.
The next layer is the calorimetry system, including an electromagnetic (ECal) and an hadronic calorimeter (HCal). The ECal got distinct active and passive mediums being liquid Argon for the active one and lead for the passive one. The material for the HCal differs by the region in the detector. It uses scintillators in the barrel and liquid Argon in the end caps as an active medium.
The outermost layer makes use of this to precisely measure properties of muons. Because they have a low ionisation rate they propagate through all the other detector layers.

4. The Top Quark and how to Reconstruct it

4.1. Top Quark Physics

The top quark is of special interest for this thesis. It is the most massive elementary particle know today with $m_t = (172.56 \pm 0.31)\,\text{GeV}$ [2]. The decay width of the top quark is $\Gamma = 1.42^{+0.19}_{-0.15}$ [2], yielding a mean lifetime in the order of $\tau \approx 10^{-25}\,\text{s}$ [2]. Because hadronisation is not instantaneous but takes place in the time span of approximately $10^{-23}\,\text{s}$ [2], the top quark is the only quark not forming bound states. Thus it provides the unique opportunity to study properties of quarks not bound in hadrons.

The top quark almost exclusively decays into a W boson and a b quark, producing a $W^-\bar{b}$ or a W^+b pair. The $W^\pm$ can decay leptonically or hadronically as described in Chapter 2.
Because a $t\bar{t}$ pair decays into $W^+bW^-\bar{b}$ there are three possibilities for the final signature in the detector. The dilepton channel is $t\bar{t} \to \ell^+\nu_\ell b\ell'^-\bar{\nu_{\ell'}}\bar{b}$ and with BR(dileptonic)$\approx 10,3\%$. It has the smallest branching ratio of the three processes. The advantage of this channel is the clear signal from the two leptons.
The second possibility is the semileptonic channel with one lepton and one jet $t\bar{t} \to q\bar{q}'b\ell\bar{\nu}_\ell\bar{b}$ or $t\bar{t} \to \bar{\ell}\nu_\ell bq\bar{q}'\bar{b}$. Its branching ratio is BR(semileptonic) $\approx 43,5\%$. The final decay channel is the full hadronic channel $t\bar{t} \to W^+bW^-\bar{b} \to q\bar{q}'bq''\bar{q}'''\bar{b}$. With BR(full hadronic) $\approx 46,2\%$ it has the largest branching ratio but it also has the largest background contributions. All decay modes are shown in Figure 4.1.

4.2. Graph Neural Networks

Machine learning (ML) has become a central tool in experimental high-energy physics (HEP). ML algorithms are already state-of-the-art in key HEP tasks such as particle and event identification, energy estimation, and pile-up mitigation. Architectures such as fully

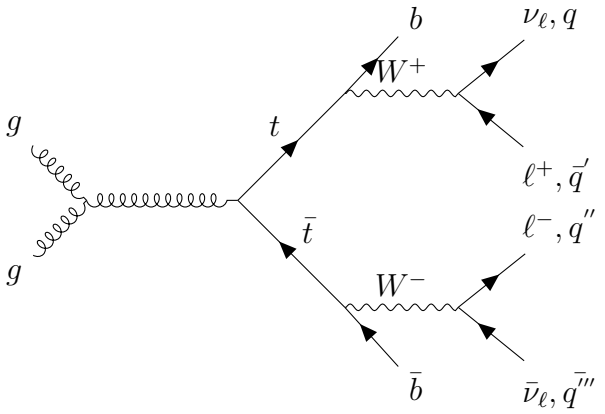


Figure 4.1.: Leading-order example Feynman diagram for the production of a $t\bar{t}$ pair and its subsequent decay. If both W bosons decay into leptons, the decay is called leptonic. If only one does, it is called a semi-leptonic decay. If both W bosons decay into quarks, it is a full hadronic decay.

connected, convolutional, and recurrent neural networks can capture complex, non-linear patterns in large datasets. A general introduction to machine learning (ML) in high energy physics can be found in [22].

Graph neural networks (GNNs) make use of a different data structure than other ML models. A graph is a mathematical structure defined as $G = (N, E)$, where N is a set of nodes and E is a set of edges that represent connections between pairs of nodes. Graphs can be directed or undirected, weighted or unweighted, depending on whether edges have direction and associated values. In GNNs, graphs serve as the fundamental input structure, where each node can have associated features represented as vectors. GNNs operate by iteratively updating node representations through a process called message passing, where each node aggregates information from its neighbours. This allows the model to capture both the features of nodes and the topology of the graph. The learned node embeddings can then be used for tasks such as node classification, link prediction, or graph classification. An example of a GNN being used in a HEP analysis is the ATLAS multi-lepton $t\bar{t}t\bar{t}$ observation paper [23], where a GNN was used for event classification.

4.3. State of $t\bar{t} + X$ Measurements in ATLAS

During Run 2 of the LHC at a center-of-mass energy of $\sqrt{s} = 13\,\text{TeV}$, the ATLAS experiment performed comprehensive measurements of top quark associated processes, providing crucial tests of the SM. The production of a top quark pair in association with the Higgs boson $t\bar{t}H$ was observed with a significance of approximately 5σ, consisten with the direct

SM Yukawa coupling of the top quark to the Higgs boson [24]. The associated production of weak bosons in $t\bar{t}+V$ proceses was also precisely measured in multilepton final states. The cross sections, $\sigma(t\bar{t}Z) \approx 0.9\,\text{pb}$ and $\sigma(t\bar{t}W) \approx 0.7\,\text{pb}$, show good agreement with SM expectations [25, 26]. These measurements provide stringent constraints on the top quark couplings to weak bosons and serve as important backgrounds for Higgs boson analyses. $t\bar{t}+\gamma$ was measured inclusively and differentially, testing the electromagnetic coupling of the top quark. The results are also consistent with SM predictions [27]. Finally, the rare production of four top quarks $t\bar{t}t\bar{t}$ was observed with a significance exceeding 5σ, yielding a cross of section $\sigma \approx 22.5\,\text{fb}$ [23]. This rare process provides unique sensitivity to physics beyond the Standard Model. Overall, ATLAS Run-2 results for $t\bar{t}+X$ events are consistent with the SM predictions while providing precise measurements of top quark couplings and rare processes.
$t\bar{t}+X$ analyses are especially interesting for studies about effective field theories (EFT) [28]. These theories add higher dimensional operators to the SM. They must be constrained through measurements. Two $t\bar{t}+X$ processes, $t\bar{t}\gamma$ and $t\bar{t}Z$, are for example sensitive to the top quarks electroweak coupling. Studies measuring both $t\bar{t}Z$ and $t\bar{t}\gamma$ together have been done for example in Ref. [29]. This study highlights the importance of joint $t\bar{t}+X$ approaches.

4.4. Current State in Top Quark Event Reconstruction

Producing vast amounts of short-lived particles, the LHC creates the problem of how to assign different objects detected to distinct particles. A framework tackling this problem is `KLFitter` [30]. To optimise certain aspects in this matter, two example ML-based algorithms, SPANet [31] and HyPER [32], will also be briefly discussed.

Kinematic Likelihood Fitter (KLFitter) In the single-lepton decay mode, which accounts for approximately 30% of all $t\bar{t}$ decays [30], the final state consists of one charged lepton, four jets of which two are b-jets, and significant missing transverse momentum. The reconstruction task requires identifying which of the $4! = 24$ possible jet-to-parton permutations corresponds to the true decay topology. The likelihood component of KLFitter evaluates all possible jet-parton assignments using transfer functions, mass constraints, and $b-$tagging information. The large number of permutations pose a problem in computational complexity. Furthermore, this complexity rises with the number of jets with $\mathcal{O}(n!)$.

Table 4.1.: Overview of three $t\bar{t}$ reconstruction frameworks that have been discussed.

Framework	**Method**	**Features**
KLFitter	Likelihood evaluation over all quark-jet permutations	Accurate assignments but computationally heavy
SPANet	Transformer network using permutation symmetry	Reduces complexity but not optimal for multi body decays
HyPER	GNN using hypergraphs	More efficient for fewer parameters slightly better performance in all-hadronic events

SPANet SPANet [31] aims to solve the problem of computational complexity. One can abstract the process of assignment with a label set $T = \{t_1, t_2, ..., t_C\}$ and an input set $X = \{x_1, x_2, ..., x_N\}$ with $N \geq C$. SPANet uses a transformer structure consisting of four stages for this. First, independent object embeddings produce latent space representations for each object, including jets, leptons, or global features like MET. Secondly, a central stack of transformer encoders learns relationships between the particles while preserving permutation symmetries. Additional transformer encoders predict which particles belong together. The last layer produces the most likely assignment and classification scores for the event.

Hypergraph for Particle Event Reconstruction (HyPER) Building on the idea of learning object assignments from sets of jets, HyPER [32] extends graph-based approaches by using hypergraphs. In contrast to an ordinary graph the edge of a hypergraph is able to connect multiple nodes at once. This allows a more natural representation of multi-body decays compared to pairwise relations used in standard graphs. Similar to SPANet, HyPER learns relationships between jets, but employs a message-passing network to iteratively update features and classify both intermediate candidates and full decay structures.
Despite its simpler architecture with significantly fewer trainable parameters, HyPER achieves slightly better reconstruction performance than SPANet on all-hadronic $t\bar{t}$ events. This efficiency makes it particularly well suited for scenarios with limited training data, while keeping flexibility to generalise to more complex final states.

Overview Table 4.1 summarises the three frameworks for assigning detected objects to distinct particles in top-quark pair events.

5. Machine Learning Methodology

For this thesis, events based on Monte Carlo Simulation are used to train and evaluate the model. The generated events represent the physics processes of interest within a detector simulation of the ATLAS detector under Run-3 conditions. The simulation of events is split up into different levels: Firstly, the event is simulated at parton-level. This is also called truth information, because every parameter of every parton is known. The next level of the generator is called the particle layer. Here gluons and quarks can be emitted through parton showering and further hadronise into mesons or baryons. This cannot be calculated with perturbation theory, therefore other models must be used. An example of these is the Lund- String-Model [33]. All of the used samples are generated with Powheg [34] at parton- level and the parton showers are created with PYTHIA [35]. The detector simulation for the reconstruction (reco) level is performed by GEANT [36]. The reconstructed objects used for this study include electrons, muons, jets, and missing transverse energy (MET).
The datasets for training and evaluation are split up into three categories: $t\bar{t}, t\bar{t}H$, and $t\bar{t}Z$. For the samples without a produced associated boson, there is also a differentiation between the decay modes of the W bosons produced by the decaying tops. This includes samples for the full-leptonic decay channel $W^+W^- \rightarrow \nu\bar{\ell}\bar{\nu}\ell$, the semi-leptonic decay channel $W^+W^- \rightarrow q\bar{q}\nu\bar{\ell}$, and the full hadronic decay channel $W^+W^- \rightarrow q\bar{q}q\bar{q}$. For the $t\bar{t}Z$ samples, the decay topology of the $t\bar{t}$ pair is inclusive. In the training data, the Z boson either decays into neutrinos $Z \rightarrow \nu\bar{\nu}$ or into a quark-pair $Z \rightarrow q\bar{q}$. The ttH samples are split into a full-leptonic and a semi-leptonic dataset. The Higgs boson either decays directly into a bottom quark pair $H \rightarrow b\bar{b}$, or it decays via $H \rightarrow WW^*$. The W's then decay hadronically or leptonically.

5.1. Preprocessing

To make the data suitable for machine learning, a few steps must be taken prior to the training process. The preprocessing takes the event topology and the maximum number of objects as inputs. It processes jets and leptons jointly as *objects*. In total, twelve features

Table 5.1.: Overview of labelling scheme for the edges and nodes.

Label	**Node object**	**Edge object**
0	unmatched	random
1	light quark	$t \to b\bar{q}$
2	s quark	$t \to b\bar{\ell}$
3	c quark	$W \to q\bar{q}'$
4	b quark	$H \to b\bar{b}$
5	Charged lepton	$Z \to q\bar{q}$

are defined as summarised in Table A.1. The node labels combine different MC objects into the same object via their PDG ID [2]. The node labelling does not differentiate between a particle and the corresponding antiparticle. The object can be unmatched. If it is matched, it can be matched to a light quark (up or down), a strange quark, a charm quark, a bottom quark, or a charged lepton. This labelling scheme is summarised in Table 5.1. The node features are the transverse momentum, energy, pseudorapidity, polar angle, mass, and the object's B-tagging score.

The graph is fully connected, so each node is connected to every other node via an edge. If two objects are not related to each other, the edge is labelled as a random edge. Though random edges may connect true partons. This is possible because the underlying ΔR matching is not perfect. A top with a subsequent leptonic decay of the W boson is labelled as a $t \to b\bar{\ell}$ edge. A top with a hadronically decaying W results in a triplet of two $t \to b\bar{q}$ edges and one $W \to q\bar{q}'$ edge. A H boson is represented by the edge of two b quarks that originated from the H boson. A Z boson is represented by the edge of two charged fermions $Z \to q\bar{q}/\ell\bar{\ell}$. Edges carry two features: The spatial separation ΔR of the two objects and their invariant mass m_{inv}. An overview of both edge and node labelling is provided in Table 5.1. In the following $b\bar{q}$ represents both $b\bar{q}$ and $\bar{b}q$, the same goes for the other edge labels. An example for a graphical representation of the introduced node and edge labels is given in Figure 5.1. This representation is embedded in the $\phi - \eta-$plane. Examples for the other topologies are given in Appendix D.

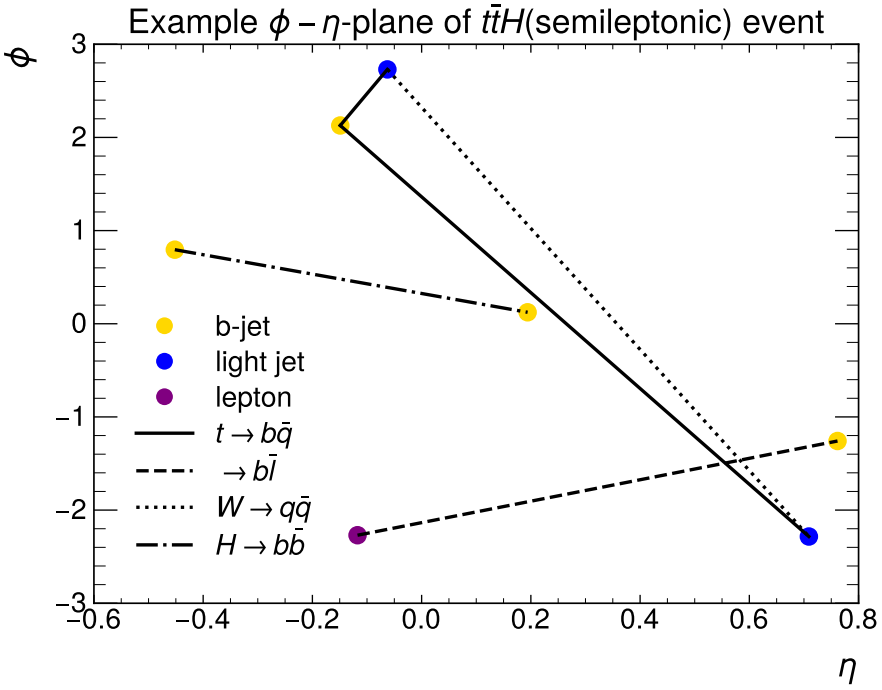


Figure 5.1.: A $t\bar{t}H$ event with a semileptonic decay of the top pair. The H decays into a $b\bar{b}$ pair.

5.2. Training the Network

The simulated events are split 80/20 into a training and a validation set. The plots are created with a third testing set. The batch size is 1000 graphs. The training set is shuffled and the validation set is not shuffled. The weights, w_{class}, for the nodes and edges are calculated with their inverse frequencies:

$$w_{\text{class}} = \frac{\text{count}_{\text{total}}}{\text{count}_{\text{class}} \cdot \text{num}_{\text{class}}}. \tag{5.1}$$

They are both evaluated using a categorical cross-entropy loss. The model consists of three networks: a node embedding MLP, a GAT, and a node classification MLP. The MLP has three layers Linear $\to$ ReLU $\to$ Linear. For the edge classification, the last MLP is changed into an edge classification MLP. The GAT has 64 hidden channels and 6 node and edge classes each and consists of four layers. Variables are normalised by $\log(\frac{x}{1000} + 1)$. The used optimiser is Adam with a learning rate of 10^{-4}. The number of training epochs is 35, and the model was trained on 910.000 events of all introduced topologies.

5.3. Loss Curve

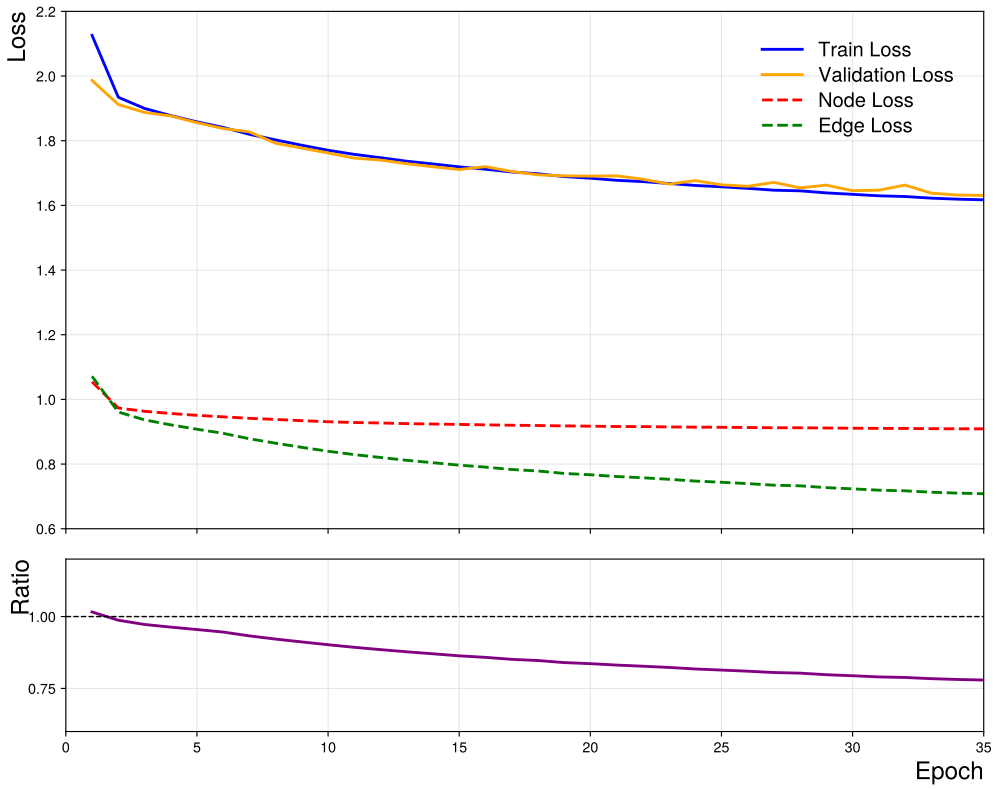


Figure 5.2.: Loss Curve of the evaluated model. On the bottom panel the ratio of the edge loss versus the node loss is shown.

The loss curve of the model is shown in Figure 5.2. The training loss and the validation loss are steadily decreasing with no apparent overfitting. The edge loss is smaller than the node loss and is still decreasing when the node loss decrease comes to a halt. Because the scores for the node classes and the edge classes are calculated with different features, it is to be expected that they differ in their performance. This is shown in the ratio panel of the plot, where it can be seen that after the first epochs the edge loss is smaller than the node loss.

6. Results

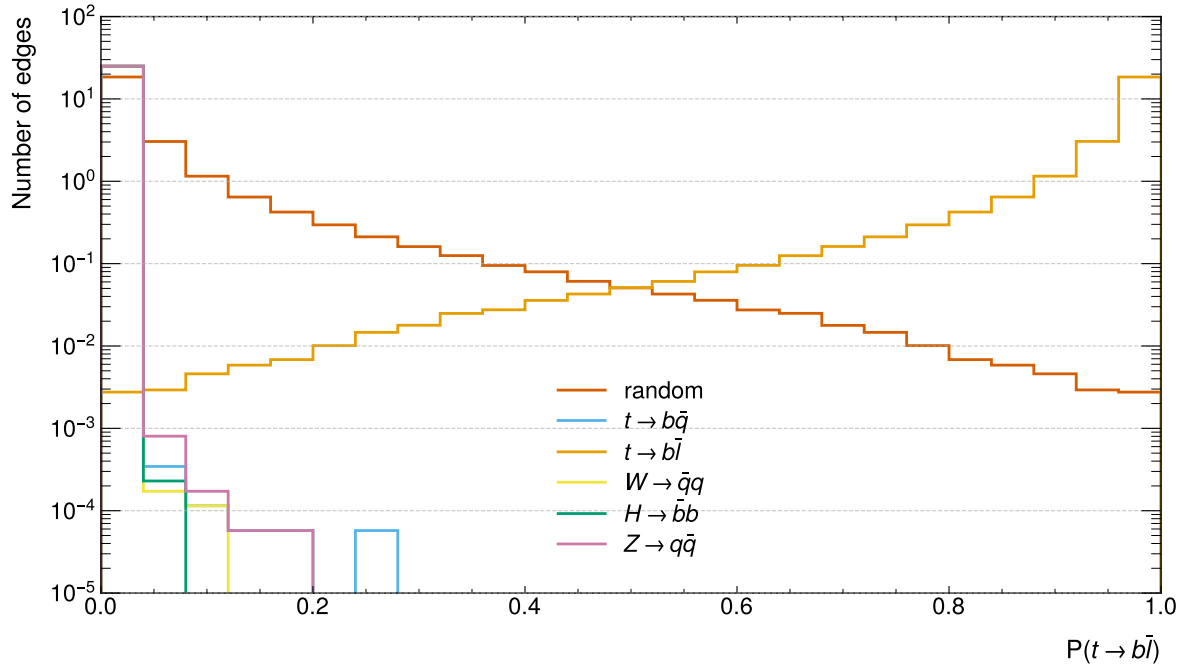


Figure 6.1.: Performance of the edge output score for the $t \to b\bar{\ell}$ class for the six different truth classes.

In this chapter, the results of this study are presented and examined. Firstly, the output scores of the model are presented for different truth topologies. Afterwards, confusion matrices of the model are presented and evaluated. They are compared with a model using only binary classification for the edges. This binary model does not distinguish between the different types of possible mother particles. It can only indicate whether two particles originated from the same mother particle. Lastly, the identification efficiency for the different partons is shown. With these values, the efficiency of reconstructing the whole event can be computed. These values are compared to other models like HyPER [32] and SPANet [31].

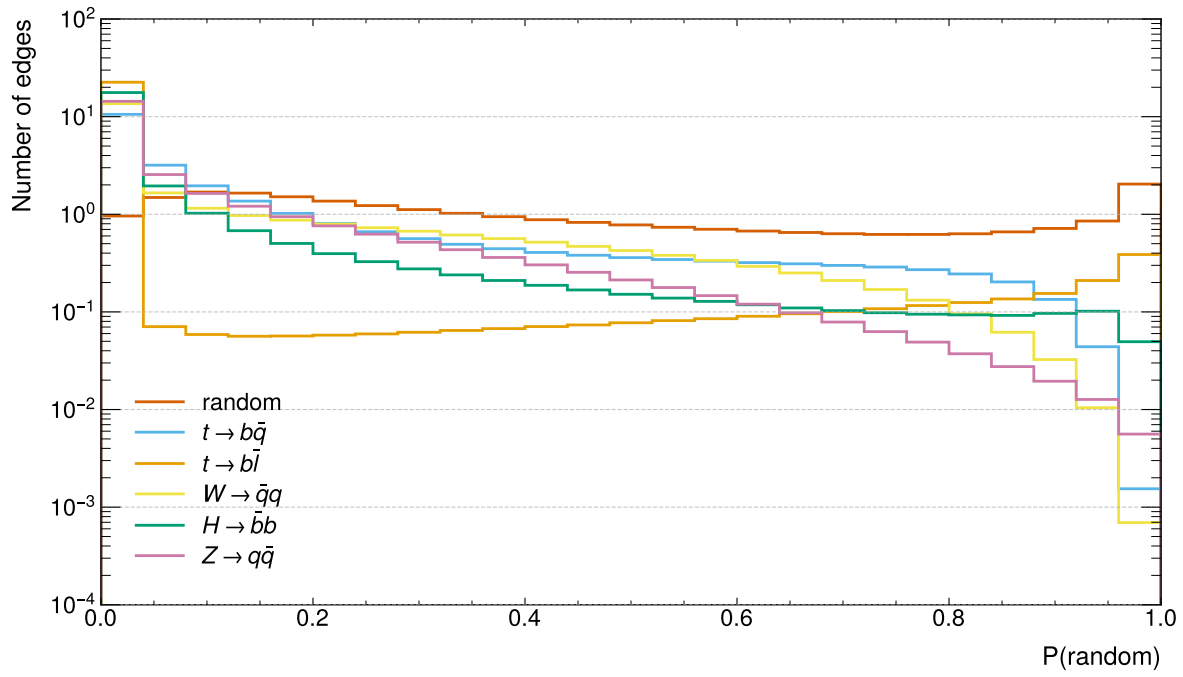


Figure 6.2.: Performance of the edge output score for the random class for the six different truth classes.

6.1. Studies of the Output Scores

For each output class, one histogram is created. It shows the score of this output value for the different truth classes. Being the classes with the lowest and highest confusion with other classes, distributions for the $t \to b\bar{\ell}$ class and for the random class are shown in Figure 6.1 and Figure 6.2, respectively. Distributions for the other classes are given in Appendix B. For each topology, the corresponding truth class has the most entries for high scores. However, there are differences in the dependence on the value of the score. For random edges and for $t \to b\bar{\ell}$ edges, the number of correctly matched edges is rising with the scores for scores larger than 0.5. The $H \to b\bar{b}$ edge shows similar behaviour but peaks in the bin immediately before the maximum score value. For the output scores for $t \to b\bar{q}$ and $W \to q\bar{q}$, the entries of the corresponding truth edge decrease for very high scores. For the $Z \to qq$ output score, the entries for the $Z \to qq$ truth edge are the least dependent on the score compared to the other truth edges.

In general truth $t \to b\bar{\ell}$ edges have very low scores in the histograms for output nodes other than random or $t \to b\bar{\ell}$ itself. And in the histogram for the $t \to b\bar{\ell}$ edge, other truth edges than random and $t \to b\bar{\ell}$ have very low scores. This will lead to lower confusion for $t \to b\bar{\ell}$ edges than for the other edges.



Figure 6.3.: Confusion matrix for the edge classes computed on all events.

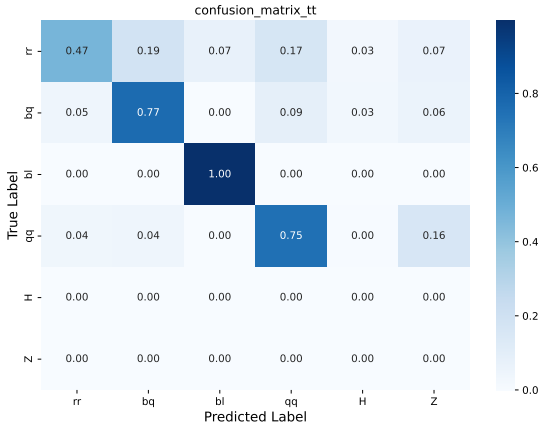


Figure 6.4.: Confusion matrix for the edge classes computed on $t\bar{t}$ events.

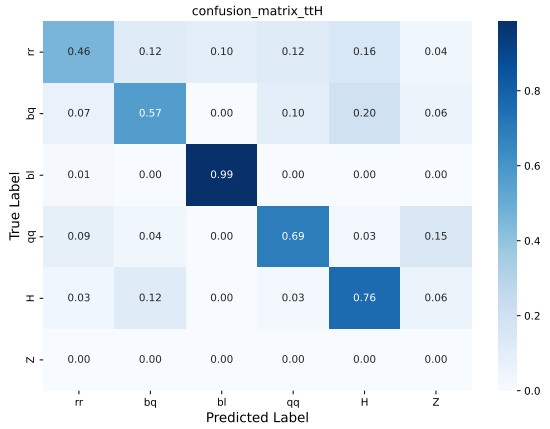


Figure 6.5.: Confusion matrix for the edge classes computed on $t\bar{t}H$ events.

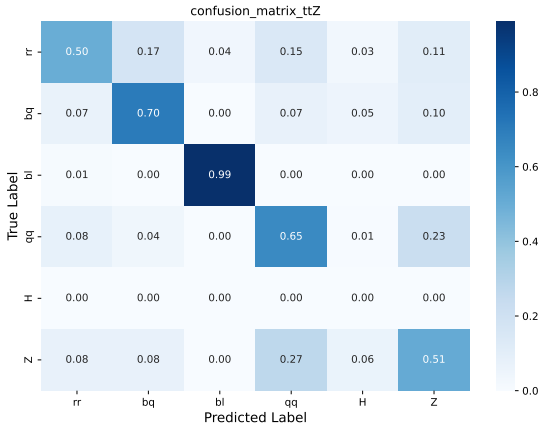


Figure 6.6.: Confusion matrix for the edge classes computed on $t\bar{t}Z$ events.

6.2. Confusion Matrices

In Figure 6.3, the confusion matrix of the edge classes for a sample containing all event topologies is shown. The chosen edge class is the class with the maximum score for this edge. The worst performance of the network is for random edges. For $t\bar{t}$, the confusion matrix is shown in Figure 6.4. Compared to Figure 6.3, every class contained in the file performs better. The rows for true $H \to b\bar{b}$ edges and true $Z \to q\bar{q}$ edges are empty, because this distribution does not include additional bosons. Though the random-random class still has the worst performance. The improvement in performance by excluding $t\bar{t}H$ and $t\bar{t}Z$ topologies indicates that poorer performance of the classification for the edges

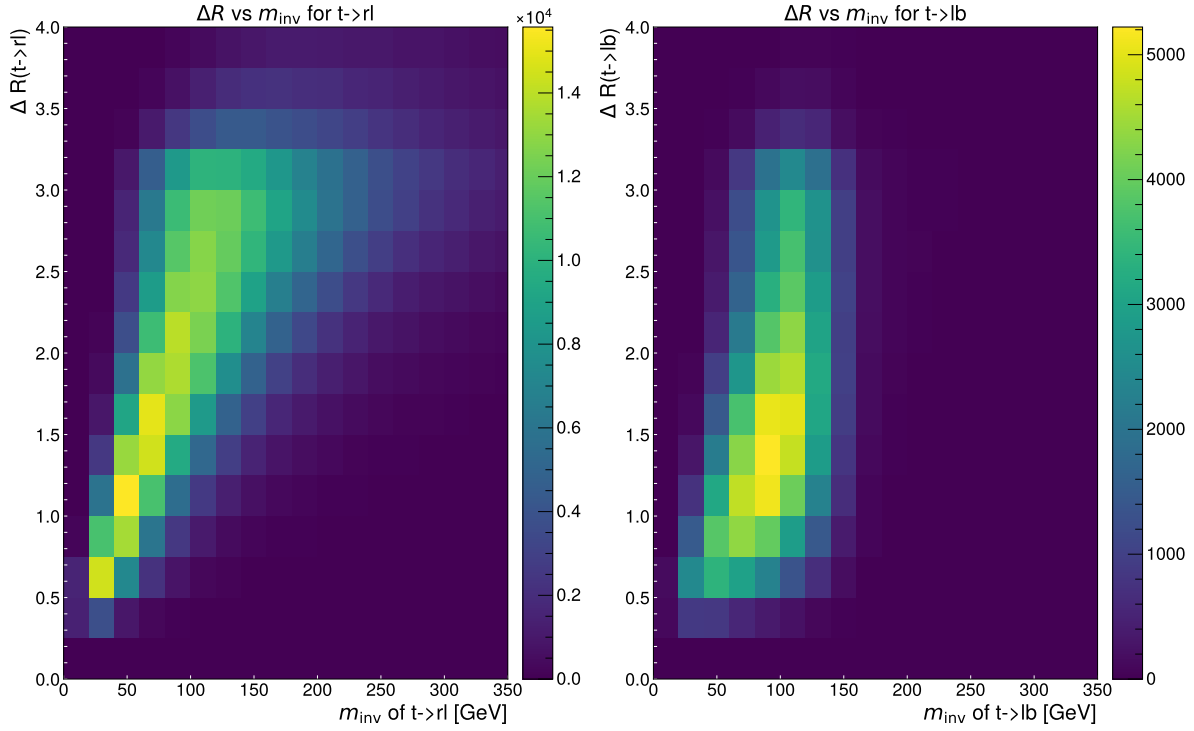


Figure 6.7.: Comparison of the edge features of $t \to bl$ edge versus a rl edge.

belonging to a top quark is most likely linked to confusion with the edge of a produced associated boson. For the topologies with an additionally produced boson, $t\bar{t}H$ and $t\bar{t}Z$, the confusion matrices are shown in Figure 6.5 and in Figure 6.6. For each topology, confusion matrices differentiating between the decay channels are shown in Appendix C. The score for the correct matching of the Higgs boson is higher than the score for the correct matching of the Z boson. In both cases the random-random edge still has the worst performance, albeit the difference in the $t\bar{t}Z$ case is only 1% compared to the correct Z matching. The Z matching has the worst performance for a non-random edge. A reason for this might be a smaller number of edges that the model could train on.

The $H \to b\bar{b}$ edge is most often confused with the $t \to b\bar{q}$ edge. The $Z \to qq$ edge is most often confused with the $W \to qq$ edge. Because they decay into the same products, this is to be expected. In Figure E.3 it can be seen that the shapes of the distributions of $W \to q\bar{q}'$ and $Z \to q\bar{q}$ are similar. Hence the model most often confuses $Z \to q\bar{q}$ with $W \to q\bar{q}'$ and vice versa.

The by far best performance for each topology is the $t \to b\bar{\ell}$ edge class with $\mathrm{P}(t \to b\bar{\ell}) \geq 0.99$ for each topology. This is most likely the case because the $t \to b\bar{\ell}$ edge is the only edge type containing a lepton. The only other possible edge containing a lepton is a random edge containing at least one lepton, resulting in an rl edge. This is the edge

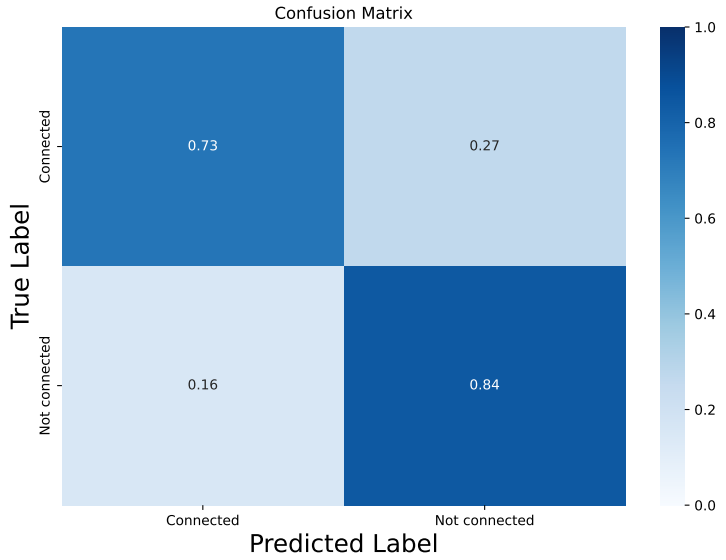


Figure 6.8.: Confusion matrix of a model using binary edge classification.

where minor confusion is happening.

In Figure 6.7, a combined comparison of the edge features as a two-dimensional heatmap is shown. The invariant mass of both edge types has peaks at around 90 GeV, although the rl edge is more broadly spread. For the spatial separation ΔR, two different peaks can be observed. ΔR for $t \to b\bar{\ell}$ edges has a peak around $\Delta R \approx 1$ and the random-lepton edges around $\Delta R \approx 3$. Normalised histograms comparing the two edge features, the spatial separation ΔR and the invariant mass m_{inv} are shown in Figure E.2 and Figure E.1.

Heatmaps for the two edge features are shown for the different truth classes in Figure E.3. The vast majority of the non-random edges are in the bins from 70 GeV up to 110 GeV. The random edges are more spread out in the $\Delta R - m_{\text{inv}}$ plane and have the most edges in the low mass region for about 30 GeV. The non-random edges also have mostly a spatial separation of $\Delta R \approx 1$, whereas the random edges are again more spread out, clustering the strongest in the bin just below $\Delta R = 1$.

The binary model used for comparison here, uses a binary classification approach for the edges instead of a multiclass approach. The confusion matrix of this model is shown in Figure 6.8. Compared to Figure 6.3, the binary classifier has a higher efficiency in classifying random edges. For non-random edges, it has a better performance than $Z \to q\bar{q}$, $W \to q\bar{q}$, and $t \to bq\bar{q}$. It performs worse than $t \to b\bar{\ell}$ and $H \to b\bar{b}$.

The confusion matrix for the node classification is shown in Figure 6.9. The best performing node class is the lepton class. The second-best-performing class is the b quark class. The worst performing class is the s quark. The highest confusion for true s quarks

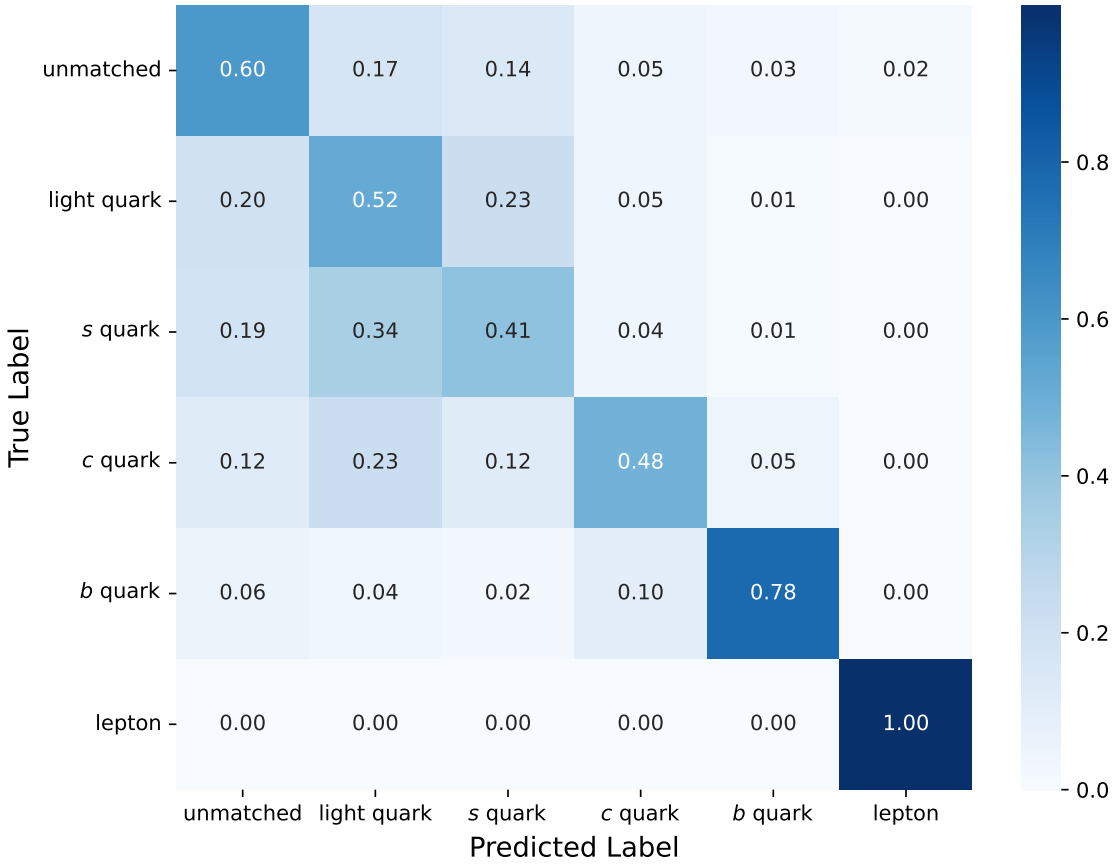


Figure 6.9.: Confusion matrix for node classification. This matrix includes all introduced decay modes.

is the confusion with light quarks. The highest confusion value is an s quark predicted to be a light quark. ATLAS has no s-tagger yet. A further improvement of the s quark classification would be of great use for future analyses.

6.3. Comparison to Other Algorithms

Playing an important role in modern analyses at CERN, there are many frameworks already implemented for $t\bar{t} + X$ event reconstruction. With a growing number of objects that must be matched, traditional approaches like KLFitter [30] or the χ^2 minimisation method become computationally expensive or have lower reconstruction efficiencies for events with high object multiplicity. Therefore, representing events as graphs is a possible approach because the relations of the objects can be learned simultaneously. To assess the quality of this approach, it is compared to ML approaches already in use like SPANet [31] and HyPER [32].

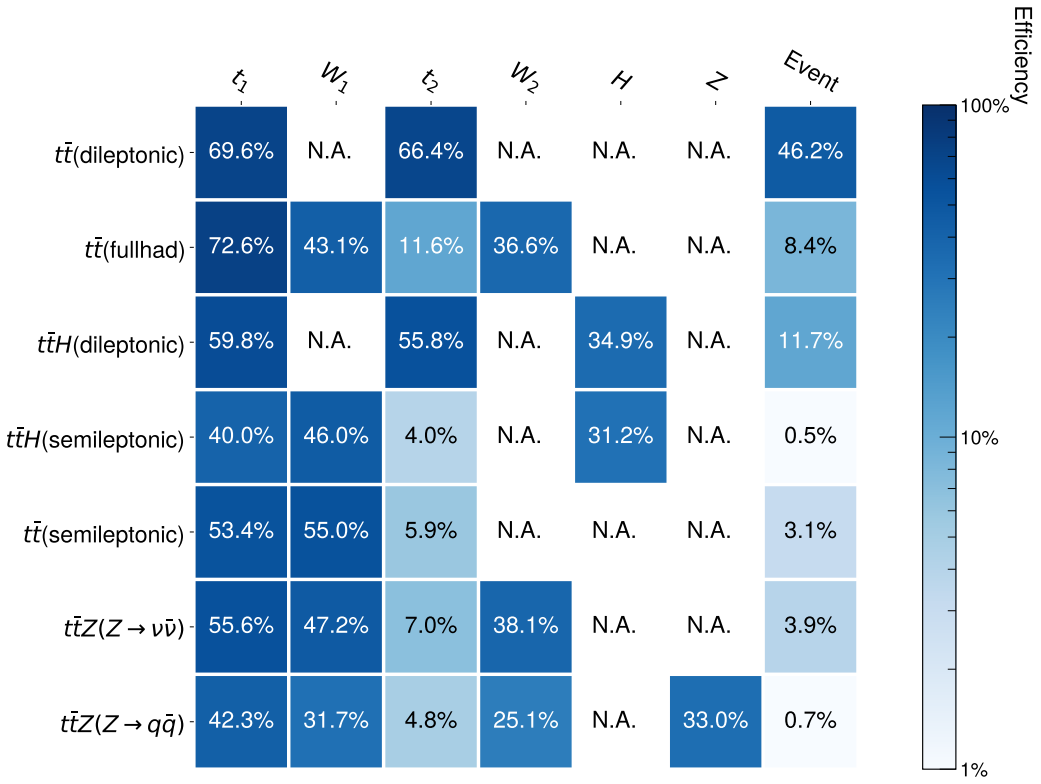


Figure 6.10.: Identification efficiency of objects in different datasets. Partons which are not produced in the decay are labelled as `N.A.`.

In Figure 6.10, the proportion of correctly classified objects for different datasets is shown. The columns represent the objects that need to be reconstructed by the network. The rows represent the different event topologies used for the analysis. If only one out of the two top quarks is reconstructed, it is matched with t_1. The same goes for the W bosons, if two W bosons can be reconstructed in this topology. Therefore $t_1 > t_2$ and $W_1 > W_2$ should always hold. For each object, the edge with the highest score for the corresponding edge class is chosen as the predicted edge. If an edge is chosen, it cannot represent another edge class to avoid double-matching. Depending on the decay topology, the top quark either decays via $t \to b\bar{\ell}$ or via $t \to bq\bar{q}$. The latter case results in a triplet such as in Figure D.3. In this case, the top quark counts as reconstructed if two out of three edges resulting from the top decay are correctly matched. For the leptonic channel, the top counts as reconstructed if the resulting edge is correctly matched. The *Event* score in the last row is the product of the reconstruction efficiencies of certain objects of this topology. An $t\bar{t}$ event is marked as reconstructed if both top quarks are reconstructed. The W reconstruction is not taken into account. For the $t\bar{t}H$ and the $t\bar{t}Z$ topologies the reconstruction efficiency of the additional boson is multiplied to the event score.

Table 6.1.: Overview of reconstruction scores for particles and events for the SPANet [31], HyPER [32], and the model used in this analysis.

Object	**SPANet**	**HyPER**	**GNN**
t quark in $t\bar{t}$	65.3%	64.4%	41.7%
t quark in $t\bar{t}H$	50.2%	-	40%
H boson	48.5%	-	31.2%
W boson	-	67.5%	43.1%
Dileptonic $t\bar{t}$ event	-	-	46.2%
Semileptonic $t\bar{t}$ event	-	-	3.1%
Fullhadronic $t\bar{t}$ event	58.6%	$(67 \pm 0.1)\%$	1.3%
Fullhadronic $t\bar{t}H$ event	33%	-	-
Dileptonic $t\bar{t}H$ event	-	-	11.7%
Semileptonic $t\bar{t}H$ event	-	-	0.5%

The best reconstruction efficiencies are achieved by t_1 for the full hadronic decay topology with 72.6%. The second and third best reconstruction efficiencies are achieved by t_1 and t_2 in the dileptonic decay of a $t\bar{t}$ pair. They achieve reconstruction efficiencies of 69.6% and 66.4%, respectively. This yields the highest event reconstruction efficiency with 46.2% for dileptonic $t\bar{t}$ events. The only other event reconstruction efficiency exceeding the 10%-percent mark is the $t\bar{t}H$(dileptonic) topology. The reconstruction efficiency is significantly reduced to 11.7% by the Higgs boson. All of the other topologies lie in the range of 0.5% to 8.4% reconstruction efficiency. The full hadronic $t\bar{t}$ sample is the only sample that can be directly compared, because both SPANet and HyPER are trained on hadronically decaying tops [31, 32]. In this sample HyPER performs the best with $(67 \pm 0.1)\%$, whilst SPANet successfully reconstructs 58.6% of the events. The model trained for this thesis reconstructs 8.4% of the events successfully. It is significantly underperforming both SPANet and HyPER. Though it has to be mentioned that, unlike SPANet and HyPER, the trained model is generic. That means that HyPER is only specifically trained on $t\bar{t}$ events without additionally produced bosons. So unlike the trained model, it cannot reconstruct $t\bar{t}H$ or $t\bar{t}Z$ events. SPANet, on the other hand, can be trained on $t\bar{t}+X$ events,

but it cannot classify multiple event topologies at once. The reconstruction efficiencies for particle classification are also shown in Table 6.1. The efficiencies are again inclusive of both fully and partially reconstructed events. If the topology features two particles of the same type, like the top quark or the W boson, the first reconstruction efficiency is compared. It can be seen that the GNN has a lower reconstruction efficiency than HyPER or SPANet in every category. But it is also important that the model actually can predict all of the classes, contrary to SPANet and HyPER both focusing on certain topologies. While still being lower, the reconstruction efficiencies for the particles lie in the same order of magnitude as the efficiencies for SPANet and HyPER. The model can also classify the nodes of the graph, not only the edges. This is an additional advantage over SPANet and HyPER.

Additionally, it has to be mentioned that HyPER was trained on 7,921,299 events [32], and SPANet on 10 million $t\bar{t}$ and 14,3 million $t\bar{t}H$ events. This is of course much more information than the 910.000 events used for the model in this work. For a more direct comparison the models would have to be trained on the same MC generated data and evaluated on the same testing set.

7. Summary and Outlook

This thesis analysed the possibility of using a generic GNN for classification tasks in $t\bar{t}+X$ processes. The basics of the SM and top quark physics have been established in Chapter 2 and Chapter 4. A brief introduction to the experimental setup of the ATLAS detector and the LHC was given in Chapter 3. Lastly, the ML methodology and the outcomes were presented in Chapter 5 and Chapter 6.

The events used for this work were simulated using MC using Run-3 settings. The selected processes included $t\bar{t}$, $t\bar{t}H$, and $t\bar{t}Z$ events with different decay topologies. The decays included dileptonic, fullhadronic, and semileptonic channels for the $t\bar{t}$ samples. The $t\bar{t}H$ samples included dileptonic and semileptonic decays of the $t\bar{t}$ pair. The Higgs is reconstructed as a $b\bar{b}$ pair. The $t\bar{t}Z$ samples are inclusive for $t\bar{t}$, and the Z boson decays hadronically or invisibly. A model predicting the flavours of objects and their relations was trained on 910000 events of different topologies. For the edges and the nodes of the GNN six classes were introduced, respectively. The node classes are: Unmatched, light quark, s quark, c quark, b quark, and lepton. The edge classes are: random, $t \to b\bar{q}$, $t \to b\bar{\ell}$, $W \to q\bar{q}$, $H \to b\bar{b}$, and $Z \to q\bar{q}$. Being trained on different features, the performance differed for edge classification and for node classification. The node and edge classification efficiencies are strongly dependent on the object type. In general, the model can reconstruct leptons and edges containing leptons, particularly $t \to b\bar{\ell}$, well. This is because the features the model trains on are more similar or more distinct for different classes. The reconstruction scores for the particles were in the same order of magnitude as the compared models SPANet [31] and HyPER [32]. The event scores were lower. The main advantage of the GNN is that it is a generic model. It can predict the scores for more particles and topologies than the already implemented work. Currently, this comes at the cost of lower reconstruction efficiency.

Although it produced lower reconstruction efficiencies than SPANet and HyPER, the GNN trained for this work gave valuable insight into new approaches to $t\bar{t}+X$ analyses. Here the model could be promising because it can learn correlations between particles that other models are not able to learn. Because EFT effects are sensitive to some $t\bar{t}+X$ topologies like $t\bar{t}\gamma$ or $t\bar{t}Z$, the model might be of use in such analyses. To compare the

result of this model to other work analysing EFTs, like this cross section measurement [29], the model could be further developed. In future work, the model can be extended to also include topologies like $t\bar{t}b\bar{b}, t\bar{t}W$, or $t\bar{t}\gamma$. Another possible extension is to also classify entire graphs into the different topologies directly with the model.

Bibliography

[1] ATLAS, CDF, CMS, D0 Collaborations, *First combination of Tevatron and LHC measurements of the top-quark mass* (2014), 1403.4427

[2] Particle Data Group, *Review of Particle Physics*, Phys. Rev. D **110**, 030001 (2024)

[3] S. L. Glashow, *Partial Symmetries of Weak Interactions*, Nucl. Phys. **22**, 579 (1961)

[4] S. Weinberg, *A Model of Leptons*, Phys. Rev. Lett. **19**, 1264 (1967)

[5] S. L. Glashow, J. Iliopoulos, L. Maiani, *Weak Interactions with Lepton-Hadron Symmetry*, Phys. Rev. D **2**, 1285 (1970)

[6] H. Georgi, S. L. Glashow, *Unified Weak and Electromagnetic Interactions without Neutral Currents*, Phys. Rev. Lett. **28**, 1494 (1972)

[7] H. D. Politzer, *Reliable Perturbative Results for Strong Interactions*, Phys. Rev. Lett. **30**, 1346 (1973)

[8] H. D. Politzer, *Asymptotic Freedom: An Approach to Strong Interactions*, Phys. Rept. **14**, 129 (1974)

[9] D. J. Gross, F. Wilczek, *Asymptotically Free Gauge Theories*, Phys. Rev. D **8**, 3633 (1973)

[10] S. Weinberg, *The Making of the Standard Model*, Eur. Phys. J. C **34**, 5 (2004)

[11] G. 't Hooft, *Renormalizable Lagrangians For Massive Yang-Mills Fields*, Nucl. Phys. B **35**, 167 (1971)

[12] G. 't Hooft, M. Veltmann, *Regularization And Renormalization Of Gauge Fields*, Nucl. Phys. B **44**, 189 (1972)

[13] G. 't Hooft, M. Veltmann, *Combinatorics of gauge fields*, Nucl. Phys. B **50**, 318 (1972)

[14] A. Belyaev, E. Boos, *Single Top Quark tW + X Production at the LHC: A Closer Look*, Phys. Rev. D **63**, 034012 (2001)

[15] N. Cabbibo, *Unitary Symmetry and Leptonic Decays*, Phys. Rev. Lett. **10**, 531 (1963)

[16] M. Kobayashi, T. Maskawa, *CP Violation in the Renormalizable Theory of Weak Interaction*, Prog. Theor. Phys. **49**, 652 (1973)

[17] P. W. Higgs, *Broken Symmetries, Massless Particles and Gauge Fields*, Phys. Lett. **12**, 132 (1964)

[18] F. Englert, R. Brout, *Broken Symmetry and the Mass of Gauge Vector Mesons*, Phys. Rev. Lett. **13**, 321 (1964)

[19] G. S. Guralnik, C. R. Hagen, T. W. B. Kibble, *Global Conservation Laws and Massless Particles*, Phys. Rev. Lett. **13**, 585 (1964)

[20] ATLAS Collaboration, *The ATLAS Experiment at the CERN Large Hadron Collider*, JINST (2008)

[21] CMS Collaboration, *The CMS Experiment at the CERN LHC*, JINST (2008)

[22] K. Albertsson, et al., *Machine Learning in High Energy Physics Community White Paper*, J. Phys. Conf. Ser. **1085(2)** (2018)

[23] ATLAS Collaboration, *Observation of four-top-quark production in the multilepton final state with the ATLAS detector*, The European Physical Journal C **83(6)** (2023)

[24] ATLAS Collaboration, *A combination of measurements of Higgs boson production in association with a top quark pair in protonâproton collisions at* $\sqrt{s} = 13$ *TeV using the ATLAS detector*, Phys. Lett. B **784**, 173 (2018)

[25] ATLAS Collaboration, *Measurement of the* $t\bar{t}Z$ *and* $t\bar{t}W$ *production cross sections in multilepton final states using 139* fb^{-1} *of* $\sqrt{s} = 13$ *TeV pp collisions with the ATLAS detector*, Eur. Phys. J. C **81**, 737 (2021)

[26] ATLAS Collaboration, *Measurement of the total and differential cross-sections of* $t\bar{t}W$ *production in pp collisions at* $\sqrt{s} = 13$ *TeV with the ATLAS detector*, JHEP **05**, 131 (2024)

[27] ATLAS Collaboration, *Measurement of the* $t\bar{t}\gamma$ *production cross section in proton-proton collisions at* $\sqrt{s} = 13$ *TeV with the ATLAS detector*, JHEP **11**, 141 (2021)

[28] CMS Collaboration, *Search for new physics in top quark production with additional leptons in proton-proton collisions at $\sqrt{s}$ = 13 TeV using effective field theory*, JHEP **2021(3)** (2021)

[29] ATLAS Collaboration, *Measurements of inclusive and differential cross-sections of $tt\gamma$ production in pp collisions at $\sqrt{s}$ = 13 TeV with the ATLAS detector*, JHEP (2024)

[30] J. Erdmann, et al., *A likelihood-based reconstruction algorithm for top-quark pairs and the KLFitter framework*, Nucl. Phys **748** (2014)

[31] A. Shmakov, et al., *SPANet: Generalized permutationless set assignment for particle physics using symmetry preserving attention*, SciPost Physics **12(5)** (2022)

[32] C. Birch-Sykes, et al., *Reconstructing short-lived particles using hypergraph representation learning*, Phys. Rev **111(3)** (2025)

[33] B. Andersson, G. Gustafson, G. Ingelman, T. Sjöstrand, *Parton fragmentation and string dynamics*, Phys. Rep. (1983)

[34] S. Alioli, et al., *A general framework for implementing NLO calculations in shower Monte Carlo programs: the POWHEG BOX*, JHEP (2010)

[35] T. Sjöstrand, et al., *PYTHIA*, Comput. Phys. Commun. **135**, 238 (2001)

[36] S. Agostinelli, et al., *Geant4 a simulation toolkit*, Nucl. Instrum. Methods A **506(3)** (2003)

A. Branches Preprocessing

Table A.1.: Overview of twelve branches exported into the preprocessed ROOT File.

Name	**Description**	**Length**
num_objects	Number of reconstructed objects n in the event.	1
obj_pt	Transverse momentum of the objects.	n
obj_e	Energy of the objects.	n
obj_eta	Pseudorapidity of the objects	n
obj_phi	Polar angle of the objects	n
obj_m	Mass of the objects	n
obj_aux	B-Tagging score of the objects	n
delta_R_flat	Difference of the angular Seperation ΔR between two opbjects.	n^2
inv_mass_flat	Invariant mass between two objects.	n^2
global_features	Missing transverse energy of the event.	2
node_label	Classifier of the flavour of the object.	n
multi_edge_label_flattened	Classifier of the flavour of the edges	n^2

B. Edge Output Scores

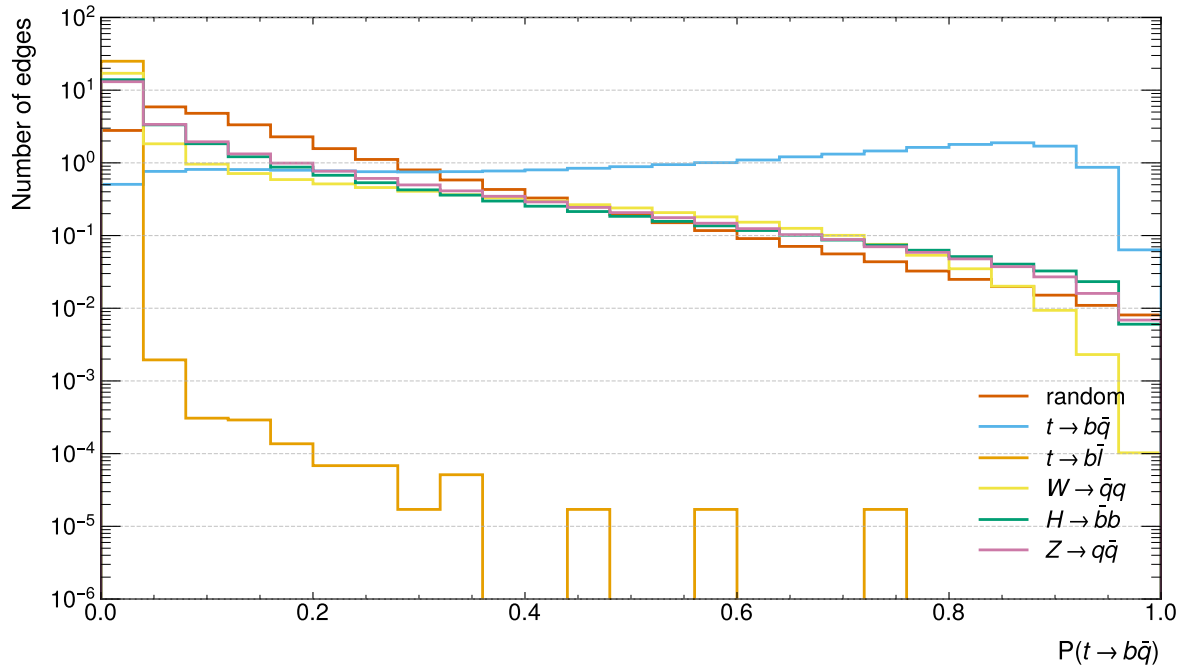


Figure B.1.: Performance of the edge output score for the $t \to b\bar{q}$ class for the six different truth classes.

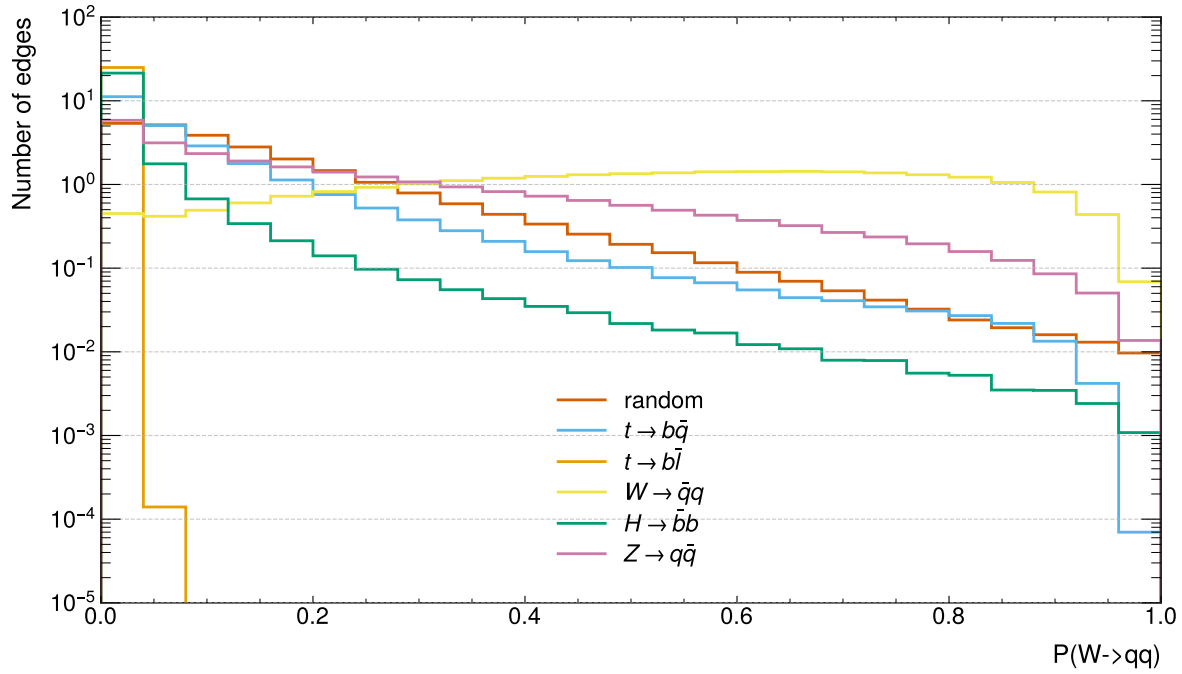


Figure B.2.: Performance of the edge output score for the $W \to q\bar{q}$ class for the six different truth classes.

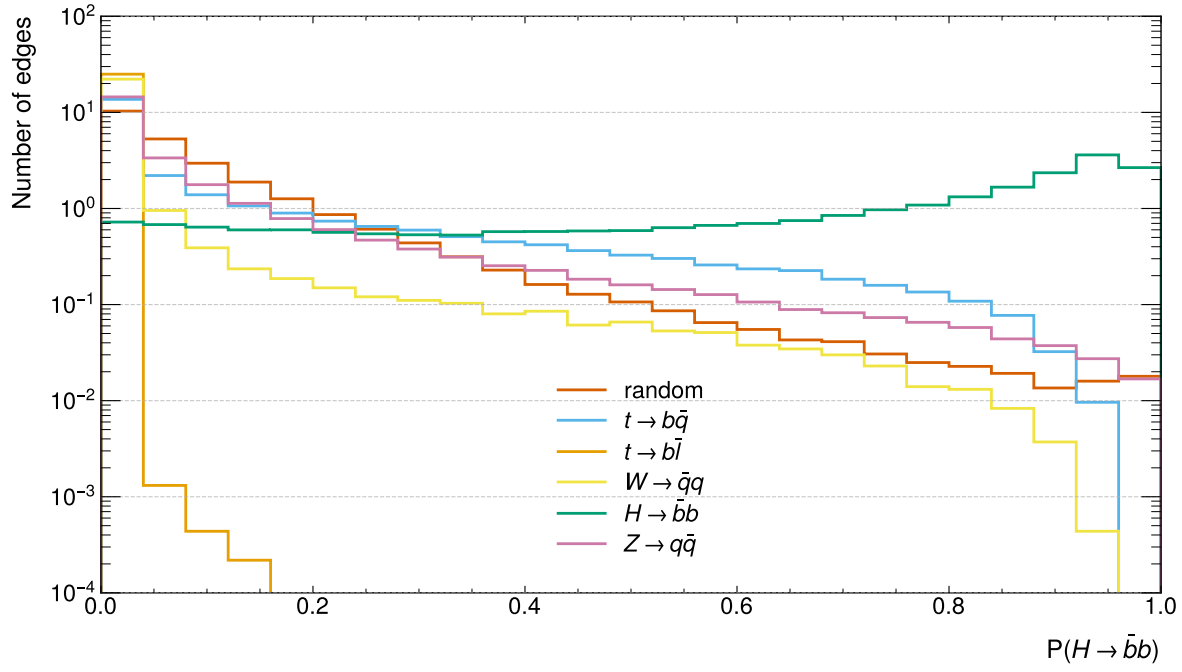


Figure B.3.: Performance of the edge output score for the $H \to b\bar{b}$ class for the six different truth classes.

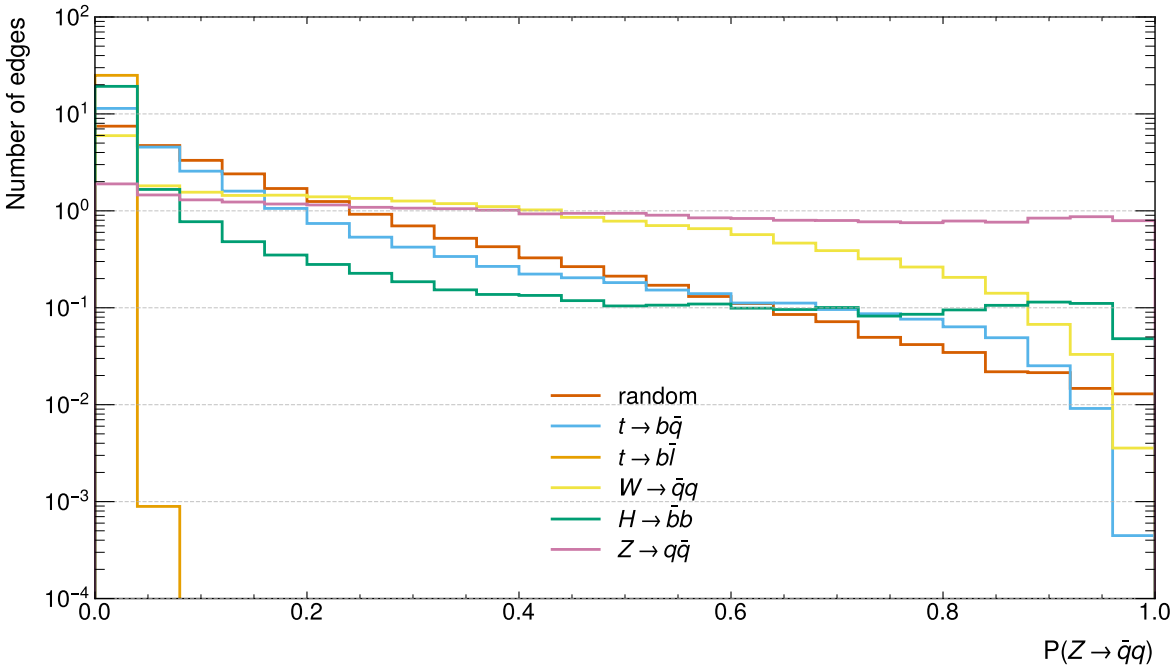


Figure B.4.: Performance of the edge output score for the $Z \to q\bar{q}$ class for the six different truth classes.

C. Confusion Matrices

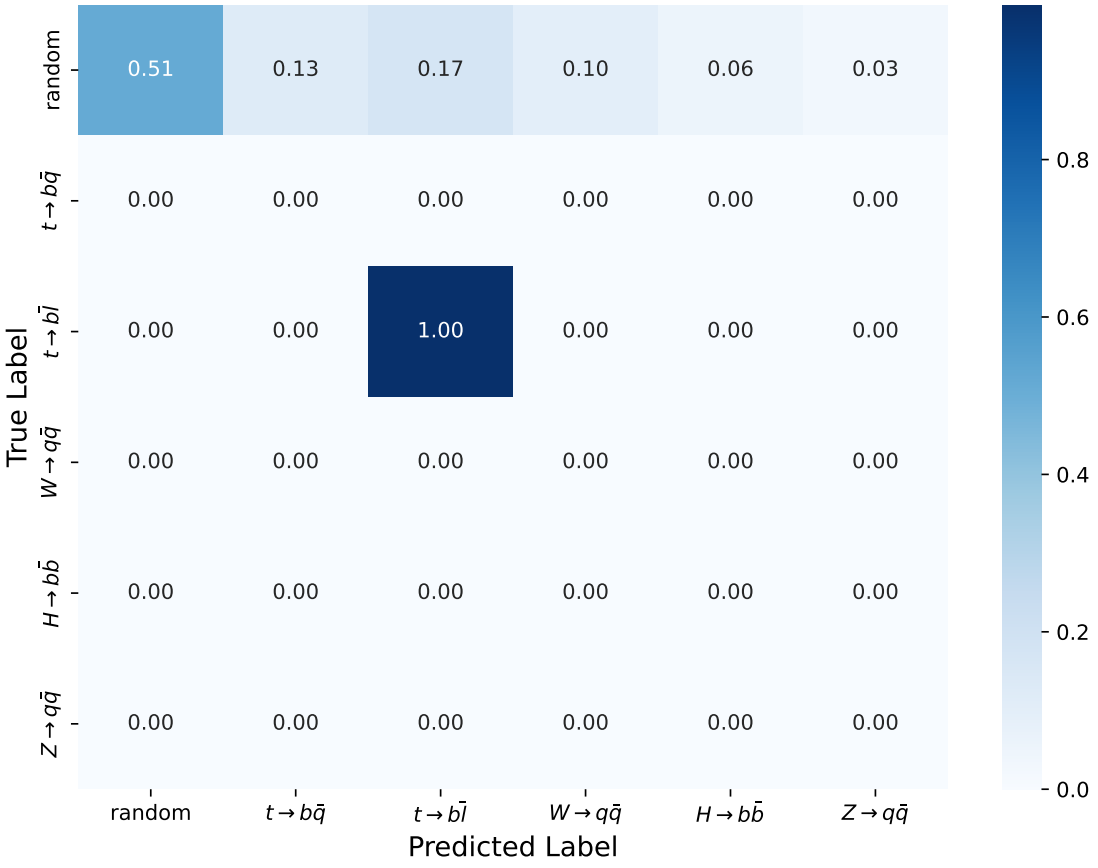


Figure C.1.: Confusion matrix computed on $t\bar{t}$ events with a dileptonic decay.

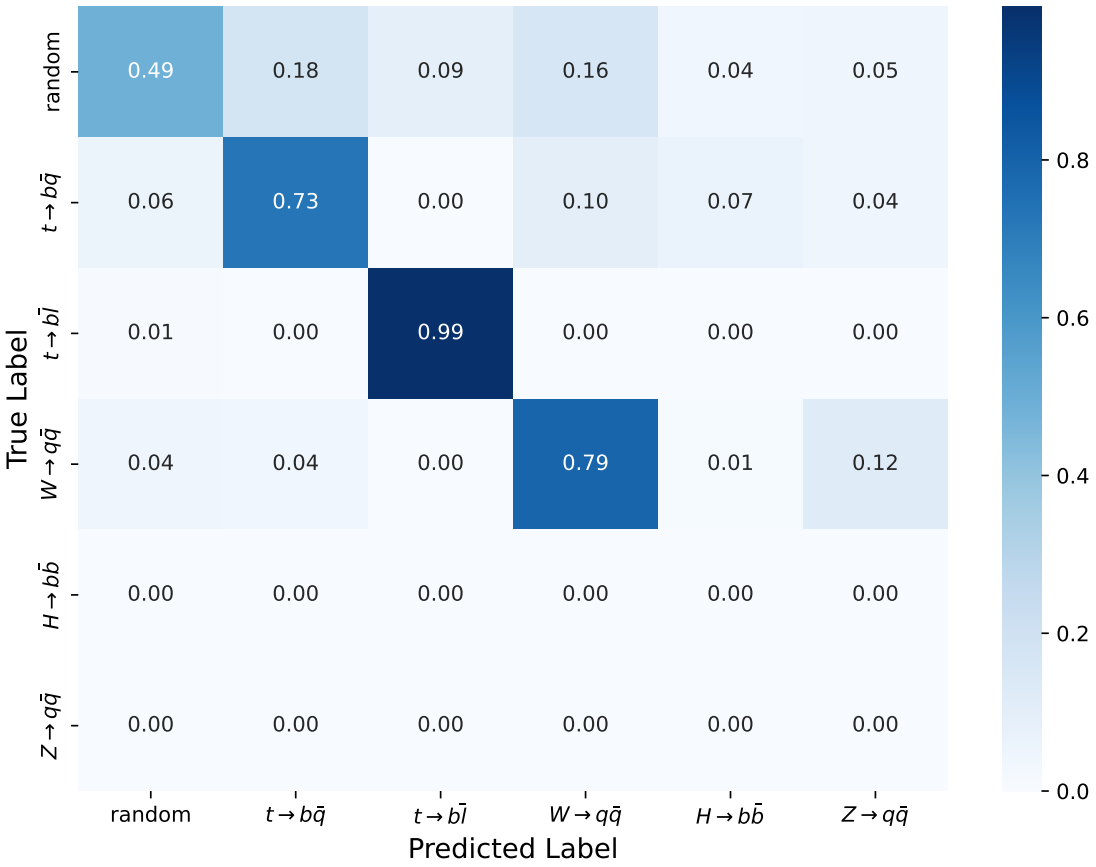


Figure C.2.: Confusion matrix computed on $t\bar{t}$ events with a semileptonic decay.

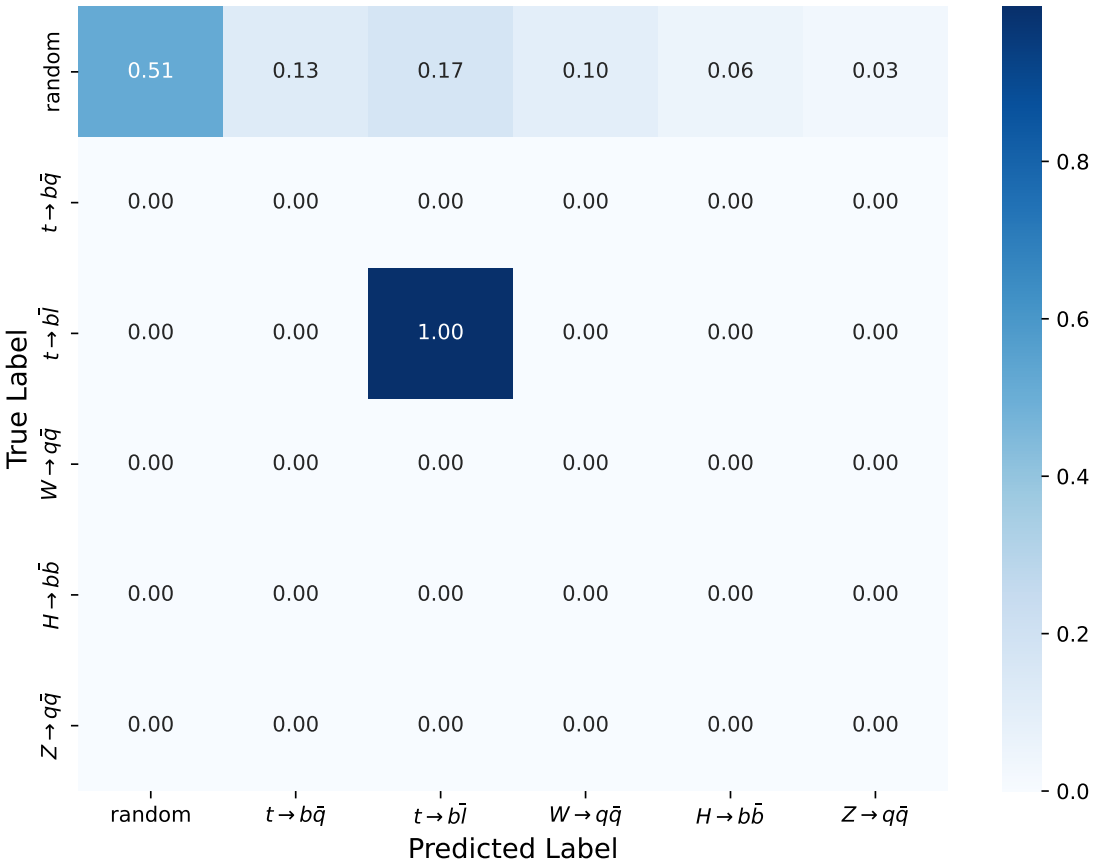


Figure C.3.: Confusion matrix computed on $t\bar{t}$ events with a full hadronic decay.

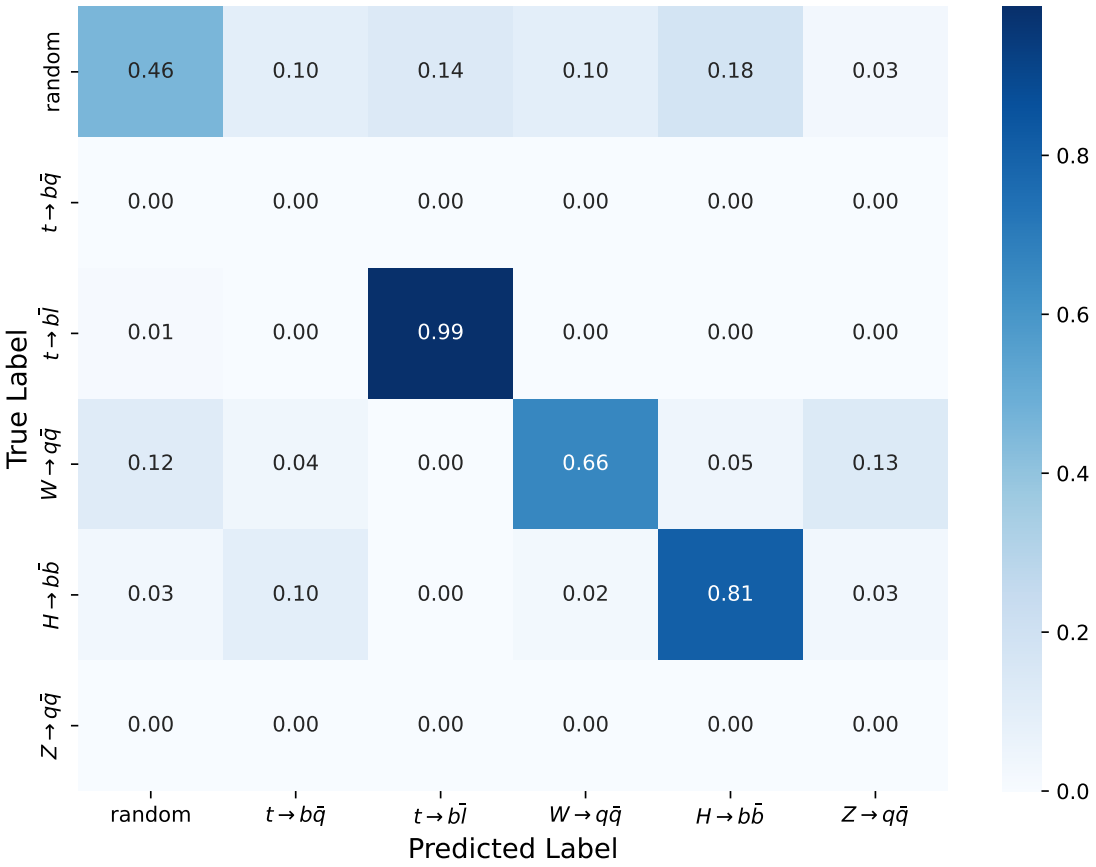


Figure C.4.: Confusion matrix computed on $t\bar{t}H$ events with a dileptonic decay.

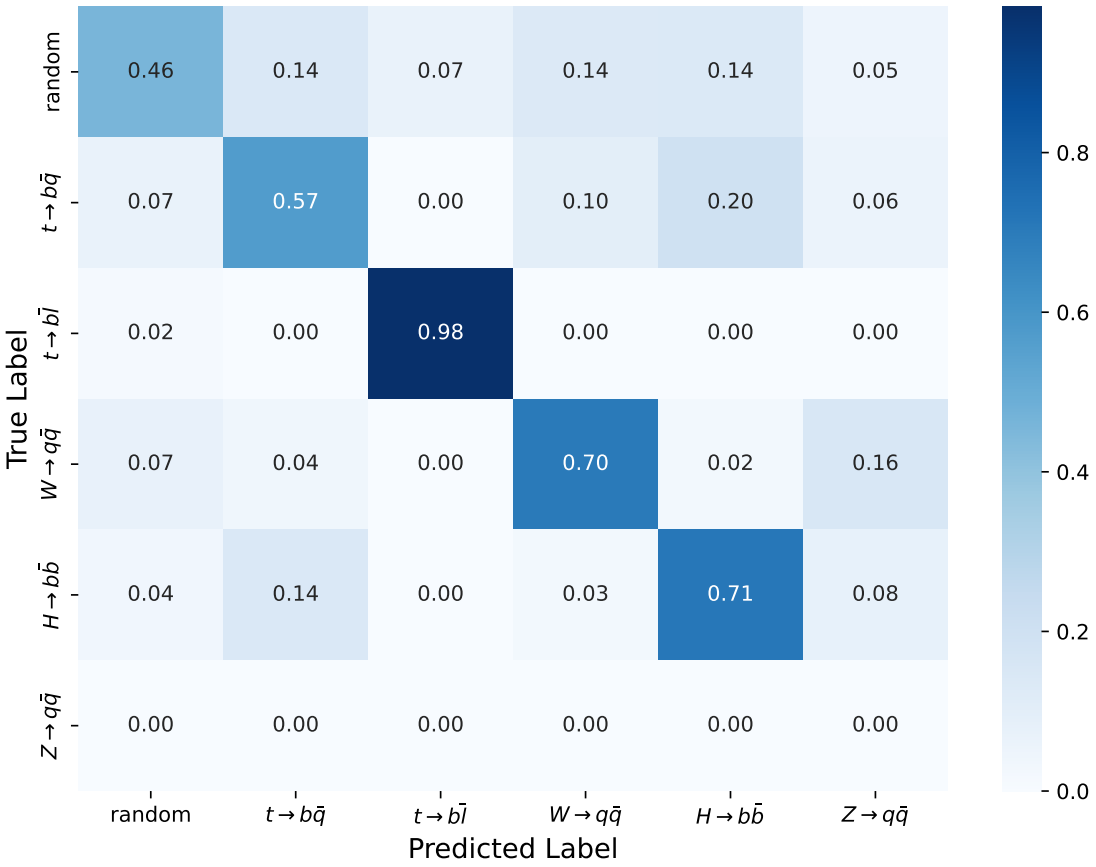


Figure C.5.: Confusion matrix computed on $t\bar{t}H$ events with a semileptonic decay.

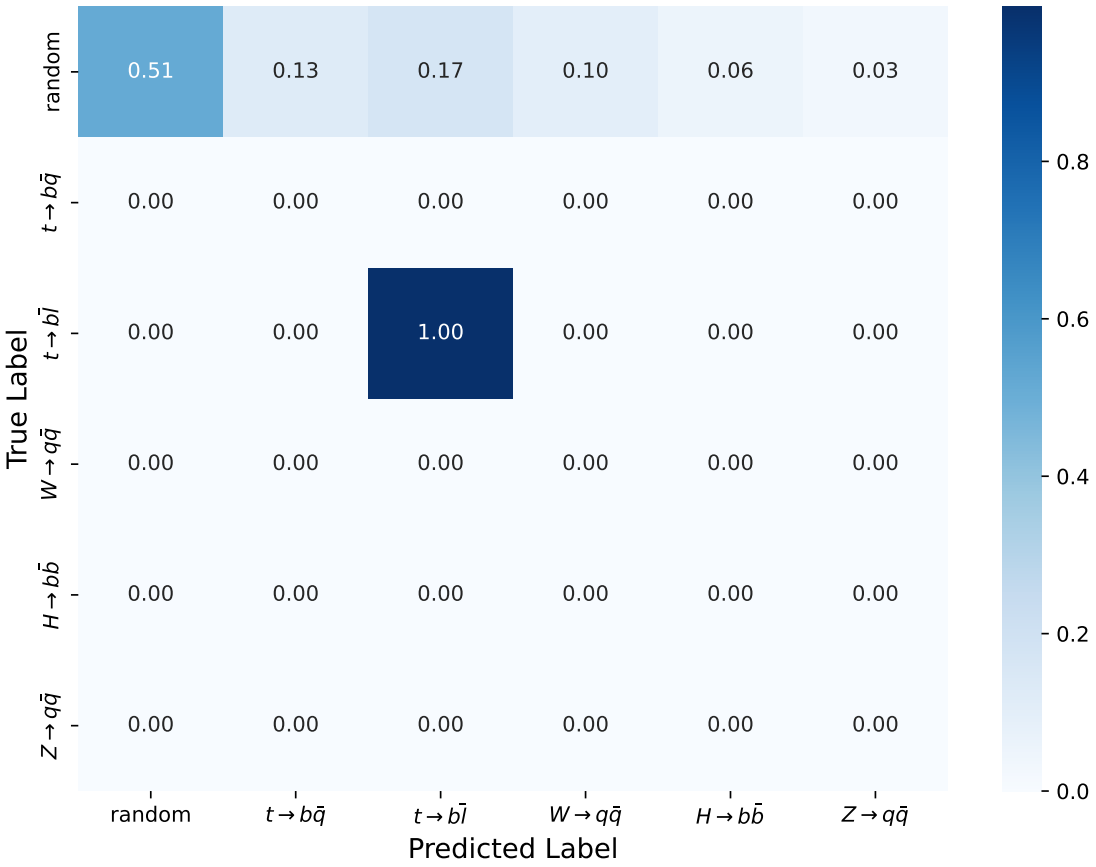


Figure C.6.: Confusion matrix computed on $t\bar{t}Z$ events with an invisible decay.

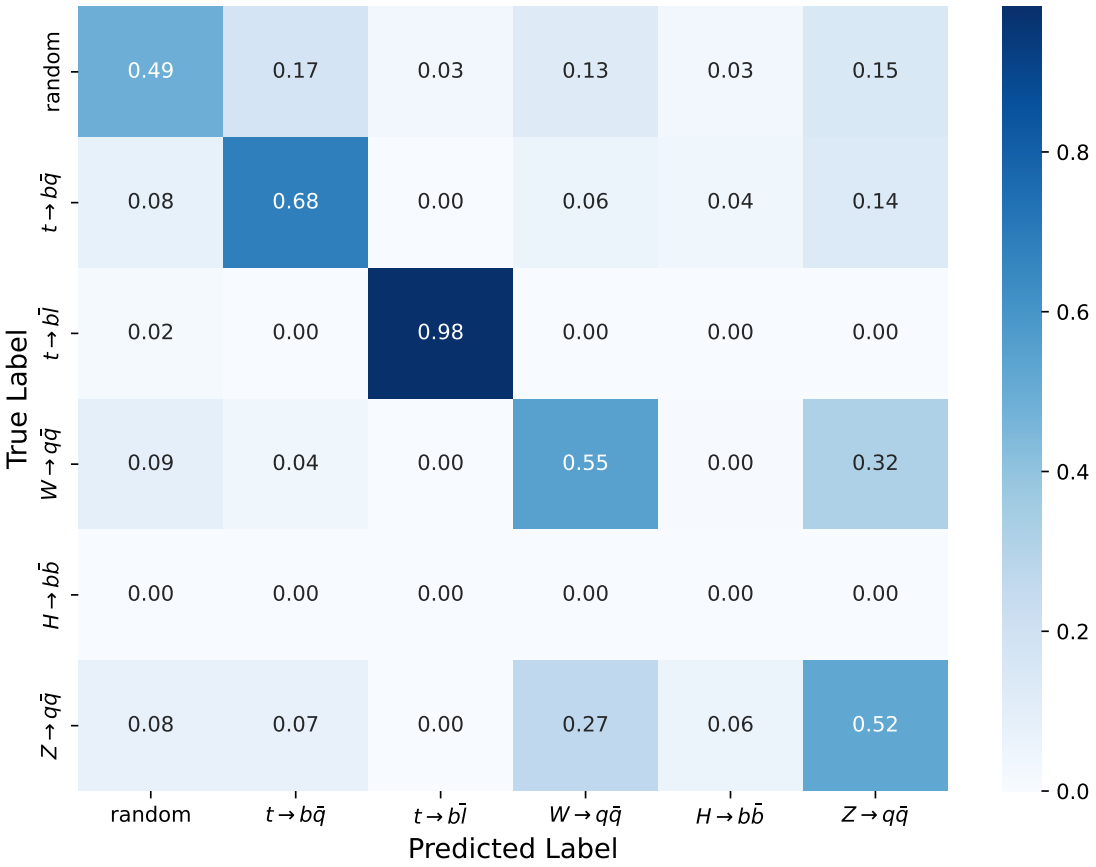


Figure C.7.: Confusion matrix computed on $t\bar{t}Z$ events with a hadronic Z decay.

D. Event Depictions

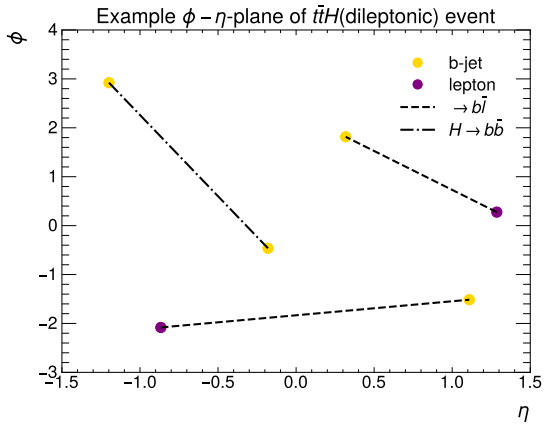


Figure D.1.: A $t\bar{t}H$ event with a dileptonic decay in the $\phi-\eta$ plane.

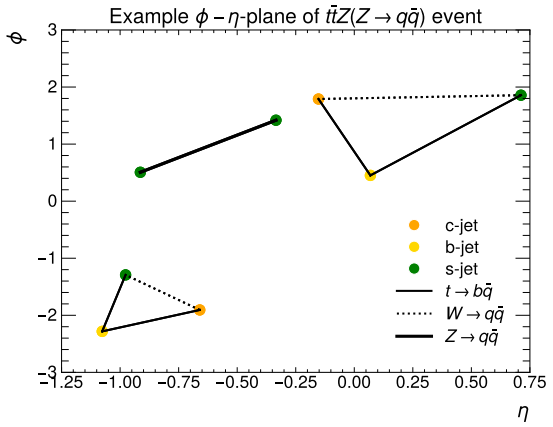


Figure D.2.: A $t\bar{t}Z$ event with a hadronic decay of the Z in the $\phi-\eta$ plane.

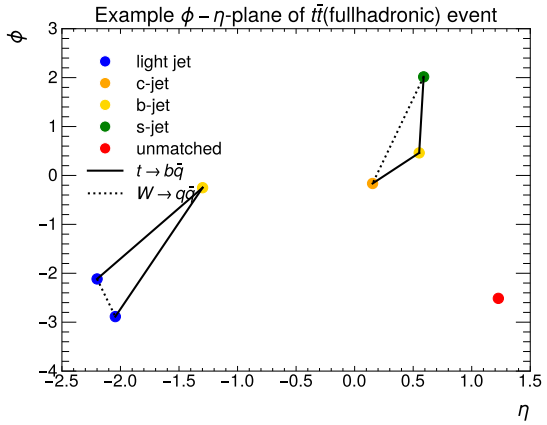


Figure D.3.: A $t\bar{t}$ event with a full hadronic decay in the $\phi-\eta$ plane.

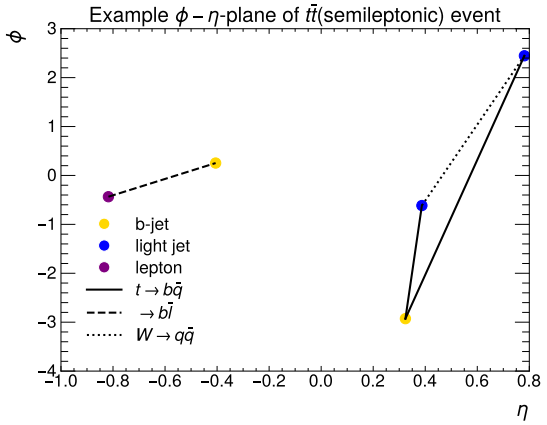


Figure D.4.: A $t\bar{t}$ event with a semileptonic decay in the $\phi-\eta$ plane.

E. ΔR and m_{inv} Distributions

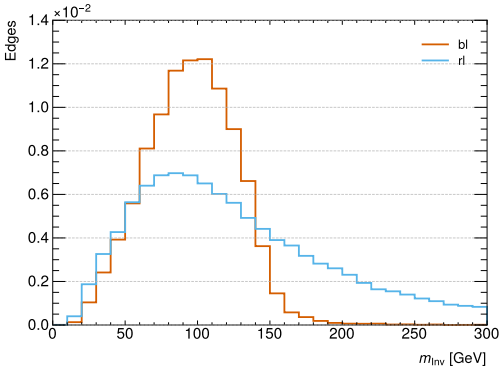


Figure E.1.: Comparison of the invariant mass m_{inv} for $t \to bl$ edges versus random edges connecting at least one lepton.

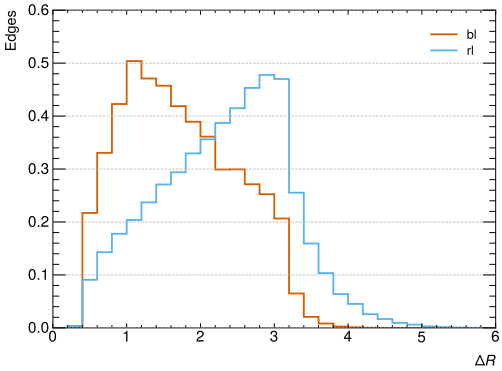


Figure E.2.: Comparison of spatial separation ΔR for $t \to bl$ edges versus random edges connecting at least one lepton.

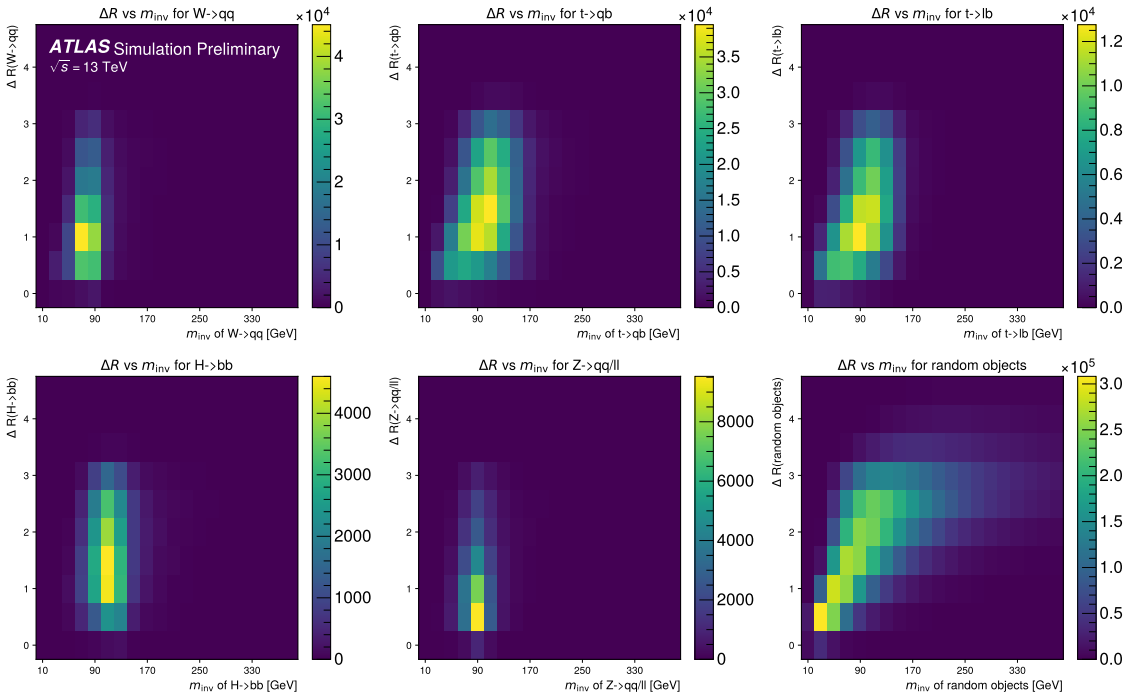


Figure E.3.: Heatmap of the different edge features for the different truth classes.

Acknowledgements

Ich möchte mich bei Arnulf Quadt für die Möglichkeit bedanken, meine Bachelorabschlussarbeit in seiner Arbeitsgruppe zu schreiben. Außerdem möchte ich mich bei Ariane Frey für das übernehmen der Zweitkorrektur bedanken.
I would also like to thank all group members who are based in Geneva and gave us a tour of the city and, most importantly, showed us around the incredible CERN site.
Im besonderen Maße möchte ich mich bei Steffen Korn bedanken. Danke dass du immer Zeit für meine Fragen hast und ich durch dein ausführliches Feedback meine Ergebnisse besser verstanden habe.
Zuletzt gilt mein Dank meiner Familie, ohne deren Unterstützung mein Studium nicht möglich wäre.

Erklärung zur Nutzung von ChatGPT und vergleichbaren Werkzeugen im Rahmen von Prüfungen

In der hier vorliegenden Arbeit habe ich ChatGPT oder eine andere KI wie folgt genutzt:

- ☐ gar nicht
- ☐ bei der Ideenfindung
- ☐ bei der Erstellung der Gliederung
- ☐ zum Erstellen einzelner Passagen, insgesamt im Umfang von _____% am gesamten Text
- ☐ zur Entwicklung von Software-Quelltexten
- ☐ zur Optimierung oder Umstrukturierung von Software-Quelltexten
- ☐ zum Korrekturlesen oder Optimieren
- ✓ Weiteres, nämlich: Spellchecker Grammarly

Ich versichere, alle Nutzungen vollständig angegeben zu haben. Fehlende oder fehlerhafte Angaben werden als Täuschungsversuch gewertet.

Mark Brandau
July 11, 2026

Erklärung nach §13(9) der Prüfungsordnung für den Bachelor-Studiengang Physik und den Master-Studiengang Physik an der Universität Göttingen:
Hiermit erkläre ich, dass ich diese Abschlussarbeit selbständig verfasst habe, keine anderen als die angegebenen Quellen und Hilfsmittel benutzt habe und alle Stellen, die wörtlich oder sinngemäß aus veröffentlichten Schriften entnommen wurden, als solche kenntlich gemacht habe.
Darüberhinaus erkläre ich, dass diese Abschlussarbeit nicht, auch nicht auszugsweise, im Rahmen einer nichtbestandenen Prüfung an dieser oder einer anderen Hochschule eingereicht wurde.

Göttingen, den 11. Juli 2026

(Mark Brandau)